

THESIS

PERIODIC METALLIC NANOSTRUCTURES FABRICATED BY COHERENT TALBOT  
LITHOGRAPHY IN A TABLE TOP SYSTEM

Submitted by

Wei Li

Department of Electrical and Computer Engineering

In partial fulfillment of the requirements

For the Degree of Master of Science

Colorado State University

Fort Collins, Colorado

Summer 2013

Master's Committee:

Advisor: Mario C. Marconi

Carmen S. Menoni  
Mingzhong Wu

## ABSTRACT

### PERIODIC METALLIC NANOSTRUCTURES FABRICATED BY COHERENT TALBOT LITHOGRAPHY IN A TABLE TOP SYSTEM

This thesis describes a novel technique of extreme ultraviolet (EUV) lithography. A compact nanofabrication system that combines Talbot lithography and a table top extreme ultraviolet laser illumination is presented. The lithographic method based on the Talbot effect provides a robust and simple experimental setup that is capable to print arbitrary periodic structures over millimeter square areas free of defects. Test structures were printed and metalized by ion beam etching system which was rebuilt and calibrated as part of this work. The results demonstrate that a complete coherent extreme ultraviolet lithographic process based on a table top system has the capability to fabricate functional periodic metallic nanostructures. Preliminary results and prospects for future work are also presented at the end of this thesis.

## ACKNOWLEDGEMENTS

I would like to thank Professor Mario C. Marconi for giving me the opportunity to work with him at the Colorado State University's Engineering Research Center for Extreme Ultraviolet Science and Technology. I would like to thank my committee members: Professor Carmen S. Menoni, Professor Mingzhong Wu and Professor Vakhtang Putkaradze for their involvement and for reading of this thesis. I would like to thank Professor Jorge J. Rocca, Dr. Weilun Chao, Dr. Aaron Stein, and Dr. Ming Lu for their valued input to this thesis. I would also like to acknowledge all my coworkers especially: Lukasz Urbanski, Ilya Kuznetsov, Dr. Dinesh Patel, Dr. Christopher G. Brown, Nils Monserud, Dr. Przemyslaw Wachulak, Dr. Brendan Reagan, Keith Wernsing, Isela Howlett, Dr. Jing Li, Michael Grisham, Dr. Fernando Brizuela, and Dr Bradley M. Luther. I would like to thank my family and my friends for their love and support.

This work was supported by the National Science Foundation, award ECCS 0901806, the NSF ERC for Extreme Ultraviolet Science and Technology, award EEC 0310717. This research was carried out in part at the Center for Functional Nanomaterials, Brookhaven National Laboratory, which is supported by the U.S. Department of Energy, Office of Basic Energy Sciences, under Contract No. DE-AC02-98CH10886.

## TABLE OF CONTENTS

CHAPTER 1	INTRODUCTION.....	1
1.1	Motivation.....	1
1.2	Pattern replication methods.....	3
1.2.1	Nanoimprint.....	3
1.2.2	Micro Contact printing.....	6
1.2.3	Scattering with angular limitation projection electron beam lithography.....	8
1.3	Non-contact EUV lithography based on Talbot imaging.....	9
1.4	REFERENCES.....	12
CHAPTER 2	TALBOT IMAGING TECHNIQUE FOR EUV LITHOGRAPHY.....	15
2.1	Experiment Set-up for Talbot Imaging.....	15
2.2	Light source review (46.9nm laser).....	16
2.3	Introduction for Talbot imaging - Talbot imaging theory.....	18
2.4	Simulation of Talbot imaging using Fresnel diffraction.....	25
2.5	Mask design and fabrication process.....	26
2.5.1	Mask design.....	26
2.5.2	Patterns generated by Jeol 6300.....	29
2.5.3	Etch process for free-standing mask.....	31
2.5.4	Results of mask fabrication.....	33

2.6	REFERENCES.....	37
CHAPTER 3 METALLIZATION PROCESS .....		39
3.1	Chemically Assist Ion Beam Etching system (CAIBE).....	39
3.1.1	Mechanism of CAIBE.....	39
3.1.2	Operation of CAIBE .....	41
3.2	Temperature control and thickness monitor system.....	44
3.2.1	Temperature control unit.....	44
3.2.2	Thickness monitor.....	44
3.3	Calibrated etching rates and stability of the system.....	45
3.4	Reference.....	48
CHAPTER 4 RESULTS OF TALBOT IMAGING .....		49
4.1	Preparations of the samples and their process procedures .....	49
4.1.1	Preparation of HSQ sample for free-standing silicon nitride masks.....	49
4.1.2	Preparation of AZPN samples for silicon membrane masks .....	51
4.2	Results of Talbot imaging .....	52
4.3	Metallization results .....	54
4.4	Analysis of the results .....	56
4.5	Future work .....	57
4.5.1	Double exposure to decrease CD.....	58
4.5.2	Sacrificial mask.....	60

4.6	Conclusion.....	62
4.7	REFERENCES.....	63
	APPENDIX 1: MATLAB CODE FOR FRESNEL DIFFRACTION .....	64

# CHAPTER 1 INTRODUCTION

## 1.1 MOTIVATION

One aspect that will promote the advancement of nanotechnology is the capability to fabricate structures with nanometer dimensions in a simple and effective manner. Hence, it is not only in the field of high volume manufacture (HVM) such as integrated circuit (IC) fabrication, but also in the field of basic research in academic and small scale industry, that nanofabrication plays an critical role. Specifically, for academic research, there are a wide range of needs for low volume nanofabrication of periodic structures, for example LED<sup>[1]</sup>, solar cell<sup>[2]</sup>, laser diode<sup>[3]</sup>, data storage devices<sup>[4]</sup>, calibration gratings, photonic crystals<sup>[5]</sup>, polarizer<sup>[6]</sup>, metamaterials<sup>[7]</sup>, nanoundulator<sup>[8]</sup>, plasmonic structures<sup>[9]</sup> or functional quantum dots<sup>[10]</sup>, etc.. These are only few examples where a low volume, fast, reliable and cost effective nanofabrication method would make a significant contribution. With the motivation to explore new alternatives, this thesis describes a defect-tolerant nanofabrication technique which is able to replicate arbitrary periodic nanopatterns from a master masks with high-resolution and high-accuracy. The method described in this work combines a classical optical effect discovered in the 19<sup>th</sup> century, Talbot imaging, with a state of the art extreme ultraviolet table top laser developed at Colorado State University to implement a new nanopatterning tool.

Talbot imaging has been used as a lithography method in the past, described as “coherent diffraction lithography”<sup>[11]</sup>. In this work we are extending its capability to the nanoscale by utilizing a state of art EUV laser source developed in CSU which enables to scale down the minimum feature size due to the shorter wavelength. The utilization of the compact EUV laser can demonstrate a cost-effective patterning tool with high-resolution that can have a significant impact in nanofabrication.

Critical dimension (*CD*) and depth of focus (*DOF*) are the two parameters that define the performance of a lithographic tool. *CD* represents the smallest feature an optical lithography system can print and *DOF* represents the necessary accuracy in positioning the sample in order to obtain a good (in focus) image or print. The two parameters are defined in equation 1-1 and 1-2 below.

$$CD = k_1 \times \frac{\lambda}{NA}; \quad (1-1)$$

In equation 1.1,  $k_1$  is a process related factor, typically equals 0.4 for production <sup>[12]</sup>, *NA* is the numerical aperture of the final lens,  $\lambda$  is the wavelength of the light used.

$$DOF = k_2 \times \frac{\lambda}{(NA)^2}; \quad (1-2)$$

Where  $k_2$  is process related factor typically equals to 2.

From equation 1-1 and 1-2 we can see that the *CD* decreases with the *NA* linearly and the *DOF* decreases with *NA* quadratically. Hence, the improvement in the *CD* by a continuous increase in the *NA* of the system has an intrinsic drawback due to the increased requirements in positioning the sample given by the decreasing *DOF* of the optical system. One effective strategy to print smaller features is then to decrease the wavelength. This is the approach followed in this work where we combined a classical self imaging effect described by Talbot in 1836 <sup>[13]</sup> with a table top EUV laser. The lithographic method described in this work is a one-to-one replication method that produces faithful replicas of a master mask. In the following sections we will review existing methods to replicate masters for which the lithographic approach described in this work can be an alternative.

## 1.2 PATTERN REPLICATION METHODS

There are several methods presently used for the replication of nanopatterns. Nanoimprint, soft lithography and electron projection lithography are few examples. Each one of them has its characteristic advantages and drawbacks which will be discussed in the following sections.

### 1.2.1 *Nanoimprint*

One method to print nano-structures and overcome the diffraction limit imposed to optical lithography is nanoimprint lithography (NIL) <sup>[14]</sup> that was proposed by Stephen Chou in 1996. This technique is based on printing the nano-structures by deformation of a polymer applying a mold on top of a layer of polymer and exerting pressure. When the resist is heated above the glass transition temperature, the low viscosity of the polymer makes it acts as a liquid. The pressure between the mold and the substrate helps the liquid fill into the details of the patterns on the mold and it holds physical shape of the polymer during the cooling cycle. After the temperature of the polymer drops below the glass transition point, the mold can be released and the patterns are duplicated onto the polymer. Nanoimprint lithography offers many advantages over conventional lithography by eliminating the need for chemical contrast created from e-beam lithography or optical lithography. It also breaks through the diffraction limit and scattering effect which are introduced by the radiation in conventional lithography. Nanoimprint lithography is basically limited only by the resolution, uniformity and stability of the polymer. Sub 10nm features <sup>[15]</sup> have been duplicated, shown in figure 1.1. This technique has widely been utilized in industrial production for feature in micron size because of its cost efficiency and its capability of copying patterns over large areas.

However, the present stage of development of this technique does not allow a high degree of uniformity compatible with the printing of defect free sub 100nm features. Although the

resolution of this technique is remarkably high (sub 10nm as shown in figure 1.1), from their results we can easily tell even the 100nm gratings are not uniform in linewidth (shown in figure 1.2). The poor uniformity is from the residual of heat and pressure in the resist during the embossing process.

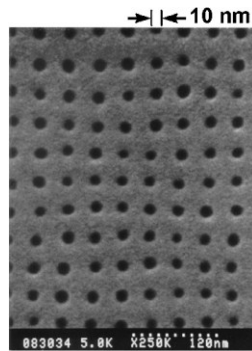


Fig. 1.1<sup>[15]</sup> 10 nm features fabricated by NIL;

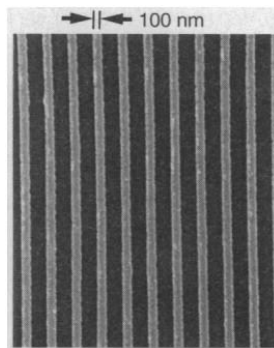


Fig.1.2<sup>[14]</sup> 100 nm gratings fabricated by NIL

The ideal alignment for the templates and polymer coated sample in NIL should be parallel to each other (shown in figure 1.3 left). However the non-uniformity caused by surface roughness of the upper-plate and backside of the sample will lead to defective imprint results (shown in figure 1.3 middle). It is also impossible for NIL to duplicate patterns on curved plates which have a wide range of application (shown in figure 1.3 right). This issue is solved by introducing air cushion press (ACP) which offers ultra uniform pressure<sup>[16]</sup> and enhances the patterning quality (shown in figure 1.4).

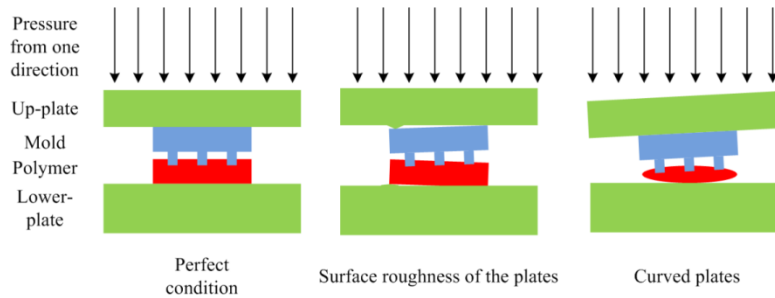


Fig. 1.3 NIL process and its limitation

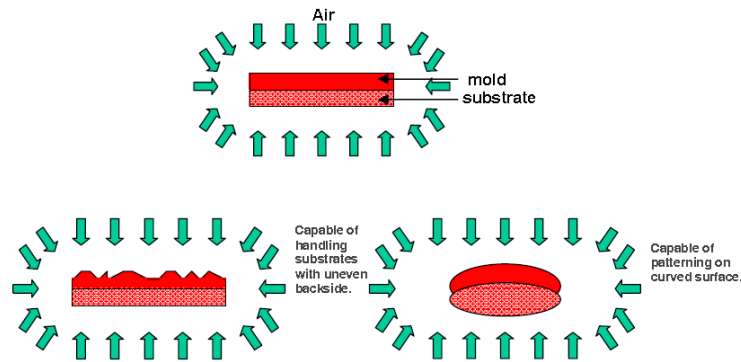


Fig. 1.4 Homogenous pressure introduced by ACP<sup>[16]</sup>

However, NIL suffers from many problems which exist in the mold releasing process<sup>[17]</sup>. To make the mold release from the sample easier, a release layer is coated on top of the mold. Despite of that, there might be a failure of adhesion between the polymer and the substrate underneath (shown in figure 1.5a). Serious defects will appear making the pattern not functional any more (shown in figure 1.5 c). In addition to that, small amount of polymer will be left to the template after NIL process (shown in figure 1.5b). This residual is very difficult to be cleaned or removed. Moreover, templates wear in NIL is worse when pressure and heat are applied. Smaller features with higher aspect ratio wear out even faster.

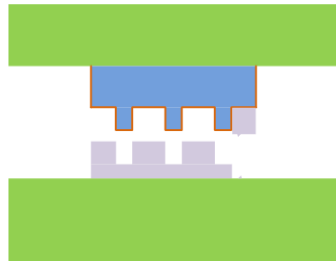
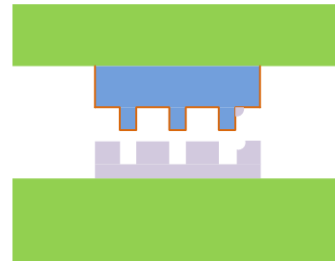


Fig. 1.5a) Defects caused by adhesion failure;



b) Mold contamination from polymer;

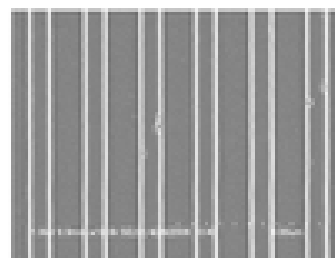
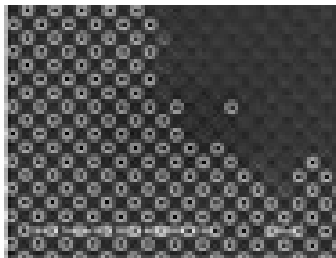


Fig. 1.5c) SEM picture of defects caused by adhesion failure <sup>[17]</sup>

### 1.2.2 *Micro Contact printing*

As a form of soft lithography, Micro Contact printing ( $\mu$ CP) is a simple, easy and cheap fabrication method which can be done in conventional environments. The mechanism of  $\mu$ CP is shown in figure 1.6. A master is prepared by traditional photolithography at first. The pattern on the master can either be in the photoresist or etched to silicon to make a more stable template. Polydimethylsiloxane (PDMS), which belongs to a group of polymeric organosilicon, is then poured on top of the silicon master. After PDMS filling all the details in the pattern on top of the silicon master, it is cured at a threshold temperature which makes PDMS into a solid elastic polymer. The PDMS master is then peeled and inked with alkanethiols. After the ink is left dry, a stamp with ink is ready to print on the substrate in form of self assemble monolayer (SAM). The inked stamp finally contacts with a metal substrate and the ink on the desired region is transferred to the top of a gold film. Hexadecanethiolate ( $\text{CH}_3(\text{CH}_2)_{15}\text{S}^-$ ) is usually formed during the SAM process. The contact time between the inked PDMS stamp and the gold substrate is

typically 10 to 20 seconds <sup>[18]</sup>. The advantages of  $\mu$ CP are obvious. Multiple uses of the silicon master and the PDMS master which has a high mechanical strength after being cross-linked <sup>[19]</sup> reduce the overall cost of this method. The elasticity of PDMS also makes the contact process easy to be applied in the industry. Several different configurations are shown in figure 1.7<sup>[18]</sup>. Other than nanoimprint in which the resist needs to be pressed and heated for more than 10 minutes,  $\mu$ CP can finish the contact process within seconds or even shorter time. Moreover, as an autophobicity chemical process, SAM can prevent the spread of transported pattern to unwanted regions which increase the density of defects. The elasticity of PDMS, on the other hand, limits the resolution registration. The sagging of elastic contact may cause uncontrolled deformation and distortion which leads to a defects density higher than the tolerated level <sup>[19]</sup>. The deformation and distortion which are not stable make the results of this technique non-repeatable. Moreover, the accuracy of  $\mu$ CP depends on SAM which cannot be performed on semiconductor substrate. It limits the application of this technique.

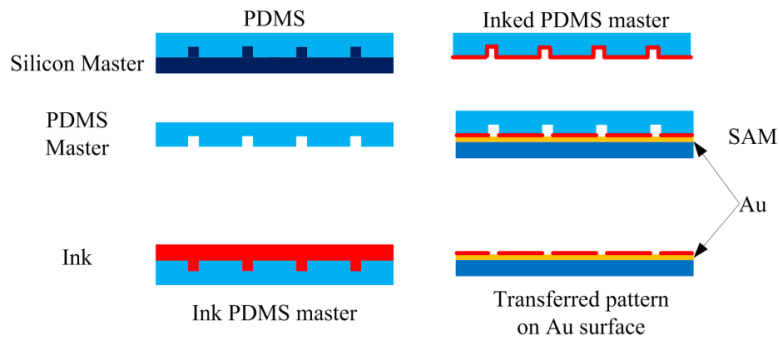


Fig. 1.6  $\mu$ CP process

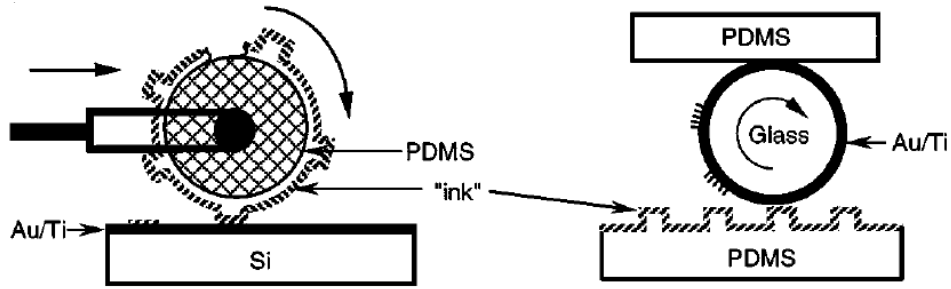


Fig. 1.7<sup>[18]</sup> another configuration for  $\mu$ CP.

### 1.2.3 Scattering with angular limitation projection electron beam lithography

Scattering with angular limitation projection electron beam lithography (SALPEL) combines the high resolution of traditional e-beam writer with the high throughput of optical projection scanner by introducing the concept of scattering with angular limitation. As the exposure source of SALPEL is an energetic electron beam, it inherits the smallest wavelength available in all the lithography techniques. As projection scanner, the duplication speed can be higher than 30 wafers per hour<sup>[20]</sup>. The main mechanism of this concept is the scattering mask rather than the traditional transmitting or reflecting and absorbing mask. The geometry of this technique is shown in figure 1.8<sup>[20]</sup>.

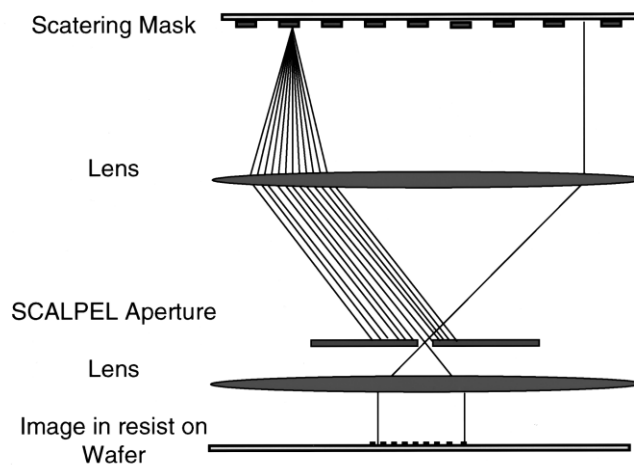


Fig. 1.8<sup>[20]</sup> Scheme for SALPEL

In fact, efforts have been devoted on projection e-beam lithography <sup>[21]</sup> since 1970s. However, the whole system suffered from the mask which absorbed the heat when energetic electrons bombard on the absorbing region intensively. The novel mask based on scattering with angular limitation <sup>[22]</sup> was developed at Bell Labs in 1990. The mask based on a membrane is completely transparent to energetic electrons so that the heat absorption is dramatically reduced. The contrast of the mask in this technique comes from the difference in the scattering angle for the patterned region made of a high atomic number material and the substrate made of a low atomic number material. The mechanism of SCALPEL is shown in figure 1.8. The pattern on the mask scatters the electrons to a larger angle and most of the scattered electrons are blocked by the SCALPEL aperture. On the other hand, the substrate which is made of low atomic number scatters the electrons to a comparative smaller angle and most of the electrons are focused to the image plane where the contrast of electrons density is thus formed.

Since the intense electron source and magnetron lens have already been available from e-beam lithography, the scattering mask makes this projection electron beam lithography methods very attractive for high volume manufacturing of sub-optical wavelength structure. However, more research needs to be done to stabilize the electron source and to circumvent the aberration of the lenses. Moreover, the throughput of SCALPEL is limited by the electron source field size which needs to be enlarged.

### 1.3 NON-CONTACT EUV LITHOGRAPHY BASED ON TALBOT IMAGING

Periodic nanostructures can also be lithographically reproduced by Talbot effect using a diode laser <sup>[23]</sup> or a deep-UV <sup>[24]</sup> illumination sources such as an ArF lasers operating at 193 nm. Dr. Urbanski <sup>[25]</sup> has also demonstrated that the combination of a compact EUV laser with Talbot lithography is capable of printing defect-free patterns in photoresist.

In this work we apply EUV lithography to create metallic nanostructures based on the Talbot imaging technique using a compact setup that incorporate with a table top EUV laser [26]. Utilizing this classical coherent imaging effect we implement a lithographic approach that allows for the replication of nano-structures on a film of photoresist with high-resolution over large areas. The process flow is shown in figure 1.9. A periodic semi-transparent mask is illuminated by coherent light. At a specific plane behind the mask, a sample coated with photo-sensitive resist is placed to record the Talbot self image and in this manner replicate the patterns on the mask. The duplicated patterns on resist are then transferred to the underlying substrate by etching process.

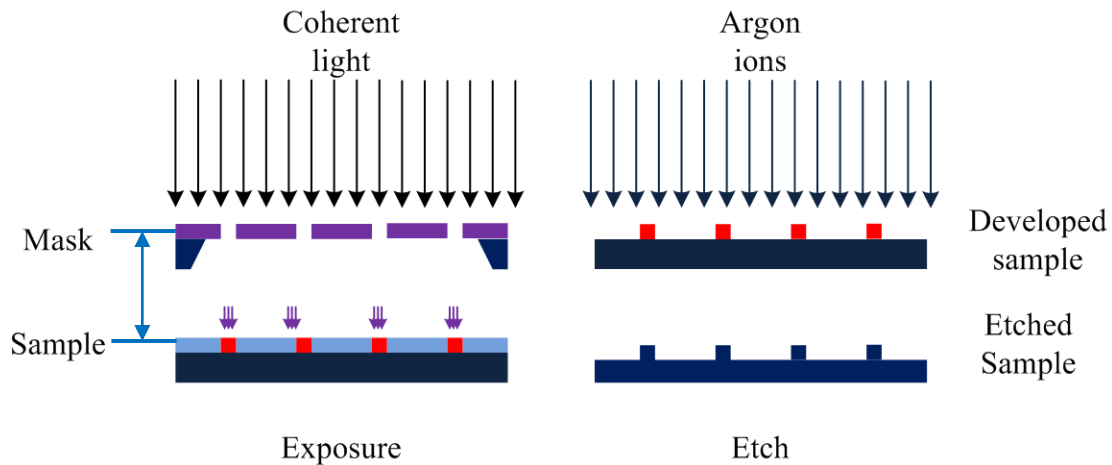


Fig. 1.9 Fabrication process flow

To implement this lithographic method we utilized a high coherent light source developed at CSU. This is a 46.9nm table top EUV capillary discharge laser. The Talbot masks were fabricated by e-beam lithography on a semi-transparent membrane. The diffractive structure of the mask generates self-images that are recorded in a photoresist and subsequently transferred to the metal layer underneath by anisotropic ion beam etching (IBE). With this technique, nano-features in metal substrate have been fabricated. The light source, the fabrication protocol for the

mask, duplication and metallization methods we used will be discussed in detail in Chapter II. After duplicating the patterns from the mask to the sample, developed nano-structures are used as sacrificial mask for the etching process subsequently (shown in figure 1.9). The etching tool used in this work is a Chemically Assist Ion Beam Etching (CAIBE) system with a hollow cathode source. The improvements made in this system and the details of the etching platform will be discussed in Chapter III.

#### 1.4 REFERENCES

- [1] Mei-Ling Kuo, Yong-Sung Kim, Mei-Li Hsieh and Shawn-Yu Lin, 'Efficient and Directed Nano-LED Emission by a Complete Elimination of Transverse-Electric Guided Modes', *NanoLetter*, Volume 11, (2011)
- [2] Hyung-Jun Koo, Yong Joo Kim, Yoon Hee Lee, Wan In Lee, Kyungkon Kim, and Nam-Gyu Park, '*Nano-embossed Hollow Spherical TiO<sub>2</sub> as Bifunctional Material for High-Efficiency Dye-Sensitized Solar Cells*', *Advanced Material*, Volume 20, (2008)
- [3] FANG QIAN, YAT LI, SILVIJA GRADEC, HONG-GYU PARK, YAJIE DONG, YONG DING, ZHONG LIN WANG 'Multi-quantum-well nanowires heterostructures for wavelength-controlled lasers', *Nature*, Volume 7, (2008)
- [4] P. Vettiger, G. Cross, M. Despont, U. Drechsler, U. Dürig, B. Gotsmann, W. Häberle, M. A. Lantz, H. E. Rothuizen, R. Stutz, and G. K. Binnig, 'The "Millipede"—Nanotechnology Entering Data Storage', *IEEE Transactions on Nanotechnology*, Volume 1, Issue 1, 2002
- [5] J.D. Joannopoulos, Shanhui Fan, '*Photonic crystal: putting a new twist on light*', *Nature*, Volume 386, Issue 6621, 1997
- [6] Kim, S H, 'Fabrication of a nano-wire grid polarizer for brightness enhancement in liquid crystal display', *Nanotechnology*, Volume 17, Issue 17, 2006;
- [7] Pendry, 'Magnetism from Conductors and Enhanced Nonlinear Phenomena', *IEEE Transaction on microwave theory and technology*, volume 47, number 11, 1999

- [8] Bellucci, S, 'New radiation sources from channeling in micro- and nano-structures', Third International Conference on Experimental Mechanics and Third Conference of the Asian Committee on Experimental Mechanics, Volume: 5852 Page(s): 276 -282, 2005
- [9] Zayats, AV, Smolyaninov, Maradudin, AA, ' Nano-optics of surface plasmonpolaritons', Physics Reports- review section of physics letters, volume 408, Issue 3-4, 2005
- [10] Daniel Lossand David P. DiVincenzo, 'Quantum computation with quantum dots', Physical Review A, Volume 57, Number 1, 1998
- [11] Christel Zanke, Minghao Qi and Henry I. Smith, 'Large-area patterning for photonic crystals via coherent diffraction lithography', JVSTB, 22(6), 2004
- [12] <http://en.wikipedia.org/wiki/Photolithography>
- [13] H. F. Talbot, 'Facts relating to optical science', Philos. Mag. 9, 1836
- [14] S.Y. Chou, P. R. Krauss, 'Imprint Lithography with 25-Nanometer Resolution', Science, Volume 279, 1996
- [15] S.Y. Chou, P. R. Krauss, 'Sub-10 nm imprint lithography and applications', JVST B, Volume 16, No. 6, 1997
- [16] H. Tan, 'Current Status of NanonexNanoimprint Solutions', SPIE, 2004
- [17] [http://www.almaden.ibm.com/st/past\\_projects/nanoimprint/defects/](http://www.almaden.ibm.com/st/past_projects/nanoimprint/defects/)
- [18] Y. Xia, G. Whitesides, 'SOFT LITHOGRAPHY', annual review material science, 1998, issue: 28

- [19] Y. Xia, G. Whitesides, 'Extending microcontact printing as a microlithographic technique', *Langmuir*, Issue 13, Page 2059-2067, 1997
- [20] L. R. Harriott, 'Scattering with angular limitation projection electron beam lithography for suboptical lithography', *JVST B*, issue: 15(6), 1997;
- [21] M. B. Heritage, 'Electron projection fabrication system', *JVST B*, issue: 12, 1975.
- [22] S. D. Berger, 'New approach to projection electron lithography with demonstrated 0.1  $\mu\text{m}$  linewidth', *Applied physics letter*, issue: 57(2), 1990;
- [23] Corey Fucetola, Amil Patel, H. Smith et al., 'Coherent diffraction lithography: periodic patterns via mask-based interference lithography', *JVST B* 27(6), 2009
- [24] H. H. Solak, Christain Dais and Francis Clube, 'Displacement Talbot lithography: a new method for high-resolution patterning of large areas', *Optical Express*, 19(11), 2011
- [25] L. Urbanski, 'Defect-free Extreme Ultraviolet nanoscale printing', *Optical Letters*, *Optical Letters*, 37(17), 2012
- [26] ROCCA, JJ; SHLYAPTSEV, V; TOMASEL, FG; et al. 'DEMONSTRATION OF A DISCHARGE PUMPED TABLE-TOP SOFT-X-RAY LASER', *PHYSICAL REVIEW LETTERS*, Volume: 73 Issue: 16 Pages: 2192-2195, Published: OCT 17 1994.

## CHAPTER 2 TALBOT IMAGING TECHNIQUE FOR EUV LITHOGRAPHY

A coherent diffraction lithography process based on Talbot imaging is described in this chapter. Nano-patterns like nano-dots and gratings were successfully duplicated with this process. The experiment set-up used for the fabrication, the light source used as exposure tool, the theory and simulation of Talbot imaging will be discussed in detail. The fabrication process for the membrane based free standing mask is also shown in this chapter.

### 2.1 EXPERIMENT SET-UP FOR TALBOT IMAGING

The geometry of the experimental set up is shown in Figure 2.1. It consists of a mask holder, a sample holder, a distance monitor, a translation stage and an actuator (pico-motor).

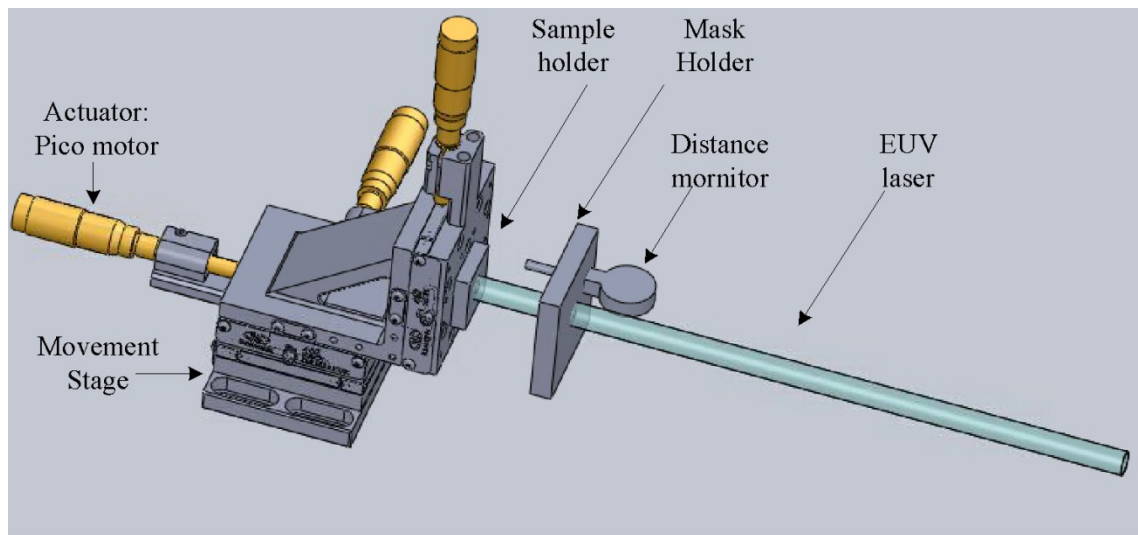


Fig. 2.1: Diagram of experiment setup.

The figure of experiment set-up is shown in figure 2.2. We first glue the mask to the slot in the holder which has a recess  $300\mu\text{m}$  deeper than the thickness of the mask. This recess is made to protect the mask from accidental contact with sample behind. A through hole on the backside of the mask holder is drilled as an opening for the EUV laser beam. Finally we zero the distance monitor and detach the sample to the calculated Talbot plane. The holders for mask and

sample are machined by computer numeric controlled milling system (CNC) which assures  $1\mu\text{m}$  flatness in the surfaces. Both the Pico-motor stage from Thorlab and the depth gage from Mitutoyo have  $1\mu\text{m}$  accuracy. The experiment set-up used in this thesis has a  $1\mu\text{m}$  resolution and repeatability.

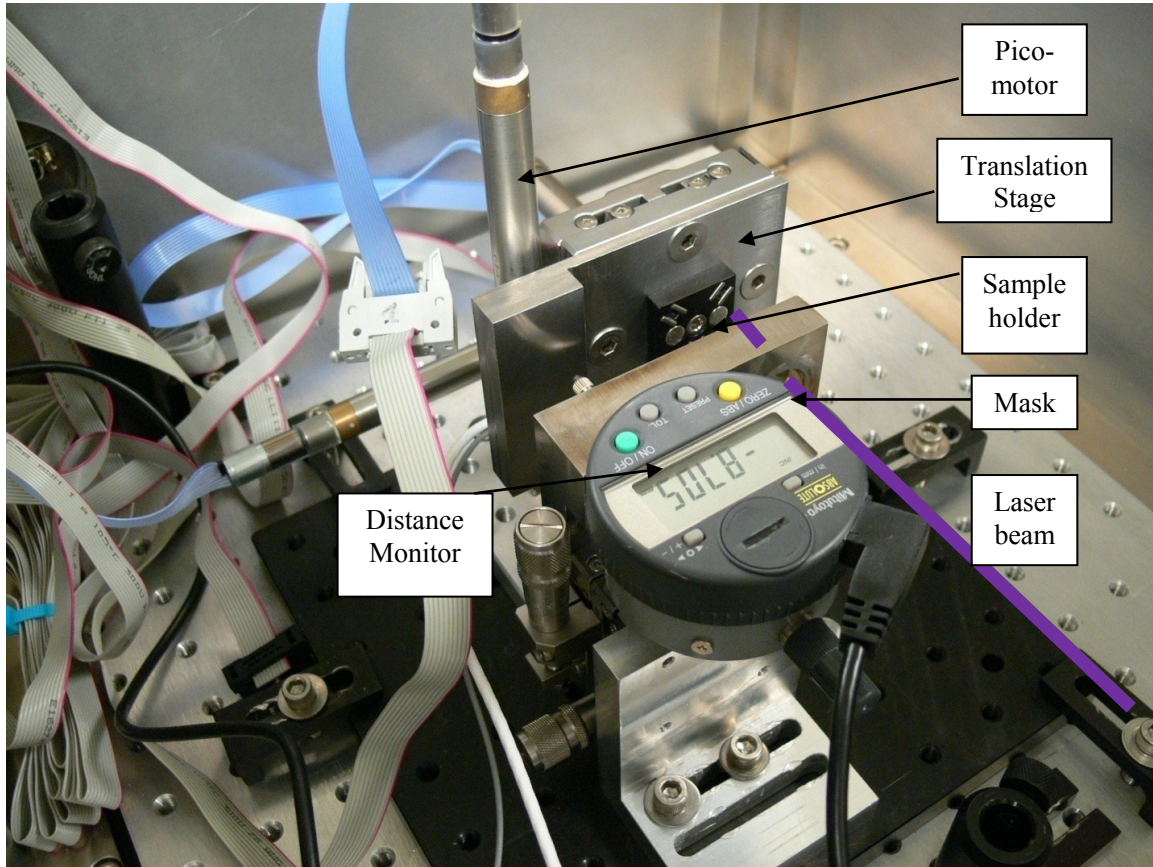


Fig. 2.2 Talbot imaging set-up

## 2.2 LIGHT SOURCE REVIEW (46.9NM LASER)

The light source used in this work is a capillary discharge laser developed in Colorado State University<sup>[1]</sup>. This table-top capillary discharge EUV laser (shown in figure 2.3) is based on hot dense plasma created by Z-pinch. A high voltage pulse is applied to both ends of an alumina capillary which is filled with 220 mTorr pre-ionized Ar gas. The current inside the capillary, which has around 22kA peak value, clamps the plasma by  $\vec{j} \times \vec{B}$  Lorenz force. The

compression leads to Z-pinch phenomenon. Population inversion and lasing action is achieved between  $1s^22s^22p^53s$  and  $1s^22s^22p^53p$  ( $J=0-1$ ), which corresponds to 46.9nm wavelength transition.

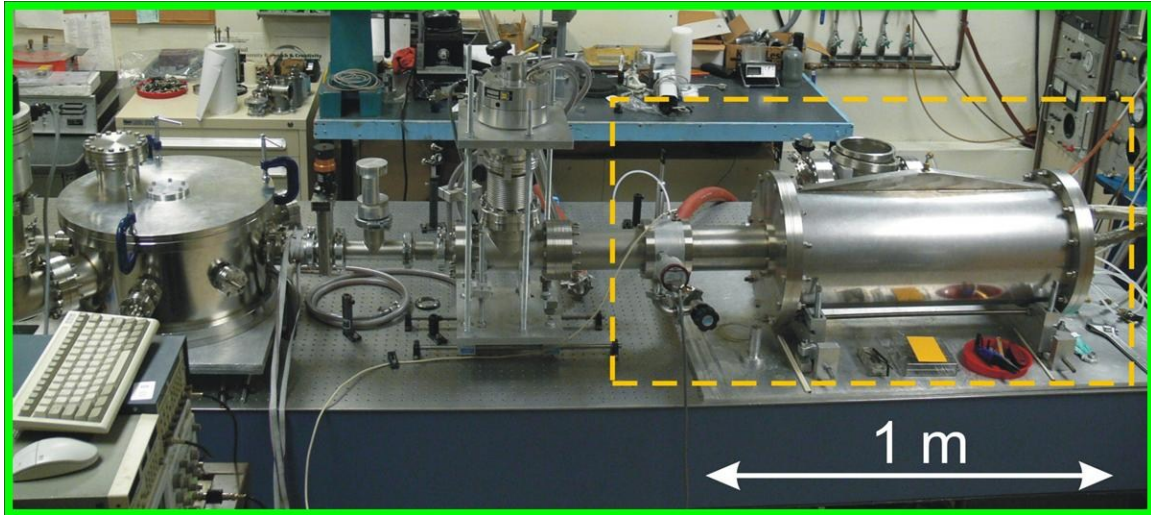


Fig. 2.3 46.9 nm Capillary discharge laser

The relative bandwidth is also very important for Talbot imaging because the focus plane is different for different wavelengths ( $Z_t = \frac{2L^2}{\lambda}$ ). Any background light or spectral far from the target wavelength will generate noise to the image. The ideal condition for the light source should be monochromatic. Figure 2.4<sup>[1]</sup> shows the emission spectrum for different capillary lengths. In a recent experiment the relative bandwidth was measured to be  $\frac{\Delta\lambda}{\lambda} = 3\sim 4 \times 10^{-5}$  <sup>[2]</sup>. The laser is also highly spatial coherent. The coherence radius is around 550um at the position where Talbot imaging was conducted <sup>[3]</sup> (2 meters away from the exit of capillary).

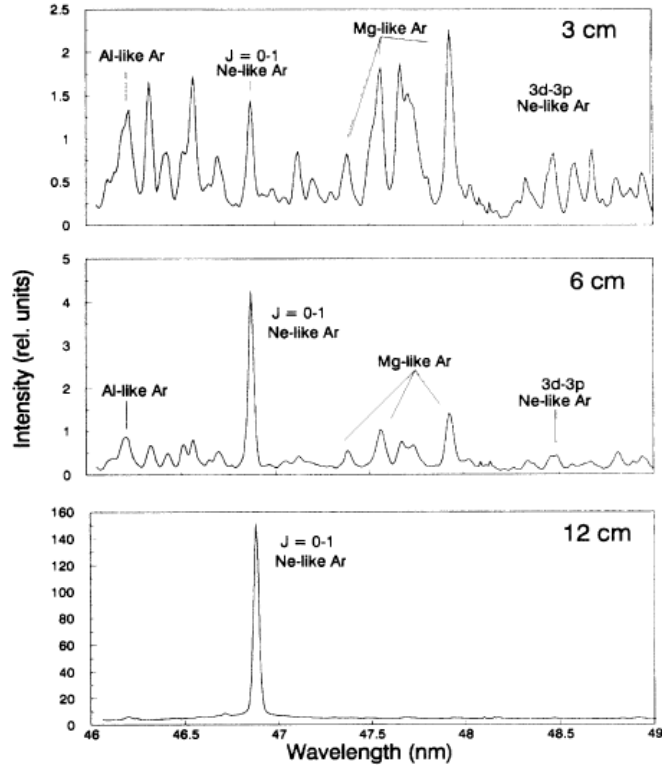


Fig. 2.4 <sup>[1]</sup> Emission Spectra for different capillary distance

### 2.3 INTRODUCTION FOR TALBOT IMAGING - TALBOT IMAGING THEORY

The fabrication method we used is based on a photolithographic step performed by self-imaging of a periodic mask, known as Talbot effect. It is actually a special case of Fresnel diffraction when a periodic mask is illuminated by a coherent light. Consider the coordinate system shown in figure 2.5.

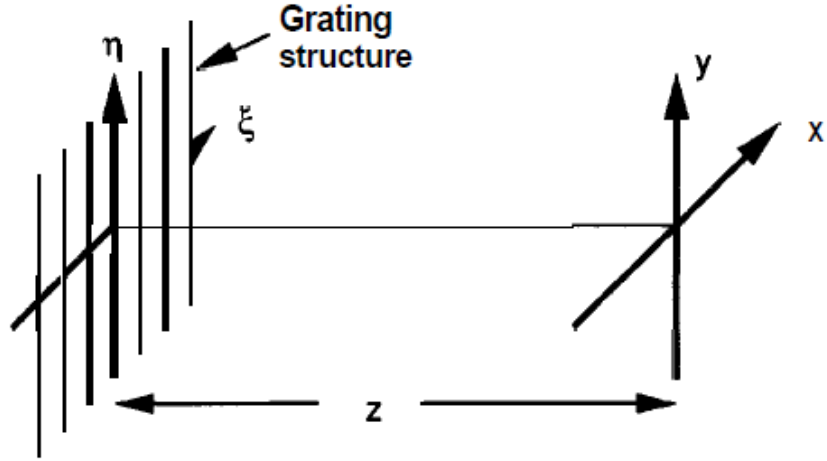


Fig. 2.5<sup>[4]</sup> Diagram for equations 2-1 to 2-9

According to Fresnel diffraction <sup>[4]</sup>,

$$U(x, y) = \frac{e^{jkz}}{j\lambda z} \iint_{-\infty}^{+\infty} U(\xi, \eta) \exp\left\{\left[\frac{jk}{2z}(x - \xi)^2 + (y - \eta)^2\right]\right\} d\xi d\eta \quad (2-1)$$

Where  $U(x, y)$  is the intensity distribution at the image plane and  $U(\xi, \eta)$  is the transmission pattern of the mask (as has been shown in figure 2.5), with kernel:  $h(x, y) = \frac{e^{jkz}}{j\lambda z} \exp\left[\frac{jk}{2z}(x^2 + y^2)\right]$ , that can also be expressed as a convolution:

$$U(x, y) = \iint_{-\infty}^{+\infty} U(\xi, \eta) h(x - \xi, y - \eta) d\xi d\eta \quad (2-2)$$

The Talbot effect is a special case of Fresnel diffraction when  $U(\xi, \eta)$  is periodic and  $z$  is in focus. Let us consider the case when the mask has a sinusoidal transmittance defined by  $t_A = 0.5 \times [1 + m \cos\left(\frac{2\pi\xi}{L}\right)]$  where  $L$  is the period of the pattern and  $m$  is the amplitude of sinusoidal signal. The Fourier transform of this periodic mask is:

$$T_A = 0.5 \times \delta(f_x, f_y) + 0.25m \times \delta\left(f_x - \frac{1}{L}, f_y\right) + 0.25m \times \delta\left(f_x + \frac{1}{L}, f_y\right) \quad (2-3)$$

The Fourier transform of the kernel:

$$H(f_x, f_y) = \exp[-j\pi\lambda z(f_x^2 + f_y^2)] \quad (2-4)$$

$$\begin{aligned} T_A \times H(f_x, f_y) &= 0.5 \times \delta(f_x, f_y) + 0.25m \times \exp\left(\frac{-j\pi\lambda z}{L^2}\right) \times \delta\left(f_x - \frac{1}{L}, f_y\right) + \\ &0.25m \times \exp\left(\frac{-j\pi\lambda z}{L^2}\right) \times \delta\left(f_x + \frac{1}{L}, f_y\right) \end{aligned} \quad (2-5)$$

The inverse Fourier transmittance of eq. 2-5 is:

$$\begin{aligned} U(x, y) &= 0.5 + 0.25m \times \exp\left(-j\frac{\pi\lambda z}{L^2}\right) \times \exp\left(j\frac{2\pi x}{L}\right) + 0.25m \times \exp\left(-j\frac{\pi\lambda z}{L^2}\right) \exp\left(-j\frac{2\pi x}{L}\right) \\ &= 0.5 \times \left[1 + m \times \exp\left(-j\frac{\pi\lambda z}{L^2}\right) \cos\left(\frac{2\pi x}{L}\right)\right] \end{aligned} \quad (2-6)$$

The intensity of this amplitude distribution can be expressed as:

$$I(x, y) = 0.25 \times \left[1 + 2m \times \cos\left(\frac{\pi\lambda z}{L^2}\right) \cos\left(\frac{2\pi x}{L}\right) + m^2 \cos^2\left(\frac{2\pi x}{L}\right)\right] \quad (2-7)$$

In eq. 2-7, if the distance 'z' is the so-called "Talbot distances" which yields  $Z_t = \frac{2nL^2}{\lambda}$ , a special diffraction patterns will be generated.

When  $Z = Z_t \frac{2nL^2}{\lambda}$ , with n an arbitrary integer:

$$I(x, y) = 0.25 \times \left[1 + 2m \times \cos\left(\frac{2\pi x}{L}\right) + m^2 \cos^2\left(\frac{2\pi x}{L}\right)\right] = 0.25 \times \left[1 + m \times \cos\left(\frac{2\pi x}{L}\right)\right]^2 \quad (2-8)$$

Eq. 2-8 has the same spatial intensity distribution as the original mask showing a perfect image of the mask which has a sinusoidal transmittance as  $t_A = 0.5 \times \left[1 + m \cos\left(\frac{2\pi x}{L}\right)\right]$ . This distance is called Talbot distance.

Or if  $Z = \frac{(2n+1)L^2}{\lambda}$ ,

$$I(x, y) = 0.25 \times \left[ 1 - 2m \times \cos\left(\frac{2\pi x}{L}\right) + m^2 \cos^2\left(\frac{2\pi x}{L}\right) \right] = 0.25 \times \left[ 1 - m \times \cos\left(\frac{2\pi x}{L}\right) \right]^2$$

This intensity distribution is a perfect image of mask with  $\pi$  phase shift.

In another case when  $Z = \frac{(n-0.5)L^2}{\lambda}$ ,

$$I(x, y) = 0.25 \times \left[ 1 + m^2 \cos^2\left(\frac{2\pi x}{L}\right) \right] = 0.25 \times \left[ (1 + 0.5 \times m^2) + 0.5 \times m^2 \cos^2\left(\frac{4\pi x}{L}\right) \right].$$

Image in this distance doubles the pattern frequency in the mask but will also decrease the contrast. With the discussion above, the Talbot planes and sub-planes can be sketched like the one in figure 2.6.

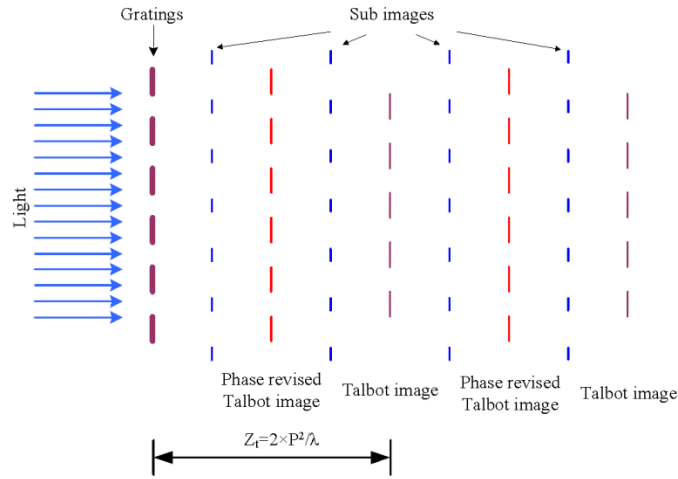


Fig. 2.6 Talbot planes & sub-planes distribution

Now let us take a deeper look of how the Talbot effect is derived from Fresnel diffraction which is actually the convolution between kernel and the transmittance function. The Fourier transform of a periodic transmittance function ( $T_a$ ) contains a  $\delta$  function, which conveys the frequency information on the mask to the image plane. This  $\delta$  function is multiplied by the

Fourier transform of the kernel function and becomes the leading behavior of intensity distribution in frequency domain when a special distance  $Z$  is applied. This means, not only the gratings with sinusoidal transmittance as  $t_A = 0.5 \times [1 + m \cos(\frac{2\pi\xi}{L})]$ , but also any mask even with 2-dimensional periodic patterns can be duplicated by Talbot image. This classic Talbot imaging effect has already been used in lithography for the duplication of photonic crystal structures which is a two-dimensional periodic pattern <sup>[5]</sup>. We generalized this coherent diffraction lithography method and made some transmission mask composed by a collection of unit cells, in which arbitrary patterns can be filled. This ‘generalized’ Talbot imaging (GTI) <sup>[6]</sup> is not limited by dots or gratings like interference lithography.

Moreover, the Talbot imaging technique has another unique character: it is defect-tolerant. This capability is shown in figure 2.7 <sup>[6]</sup>. The self-image produced by Fresnel diffraction is the collective result of the diffraction produced by thousands of tiles on the mask. If among the tiles there are some defects, these defects are averaged over the whole image adding a small noise background, but essentially reproducing the mask’s image without the defects. The non-defective tiles help to ‘fix’ the defects as long as they are not periodic consequently making this fabrication method defects-free <sup>[7]</sup>.

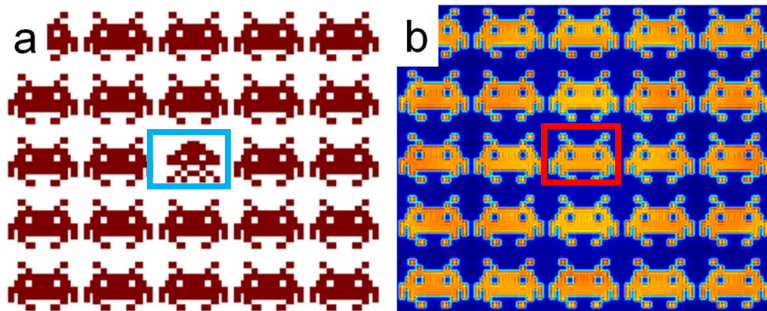


Fig. 2.7 <sup>[6]</sup> Simulation results for defect-tolerant capability based on Talbot imaging: Defect in the middle of the mask (left image) is fixed in the reconstruction image at Talbot plane (right image).

The scheme of the Talbot imaging system is shown in figure 2.8 [8]. The requirements of this method can be summarized as: a high coherent light source, a periodic mask and an accurate distance control between the mask and the sample. The Talbot distance  $Z_t$  depends on the wavelength of the light source ( $\lambda$ ) and the period of the patterns on mask ( $L$ ) as  $Z_t = \frac{2nL^2}{\lambda}$ , where  $n$  is integer. The optical resolution can be expressed as:

$$Res = \frac{0.61*\lambda}{NA} = \frac{0.61*\lambda}{\tan^{-1}(0.5*\frac{a}{Z_t})} \quad (2-9)$$

Where, “a” is the size of the mask that is assumed to be square. This equation is plotted in figure 2.9 which shows how the Talbot distance and the resolution are related to the wavelength of the light source and the period of patterns in mask. It is obvious that, with the same wavelength, the larger period leads to longer Talbot distance, which can make the experiment easier, but also decreases the resolution. On the other hand, with the same period in the mask, the smaller wavelength leads to longer Talbot distance and higher resolution. With this analysis, we can conclude that, a shorter wavelength will give a better result for Talbot lithography.

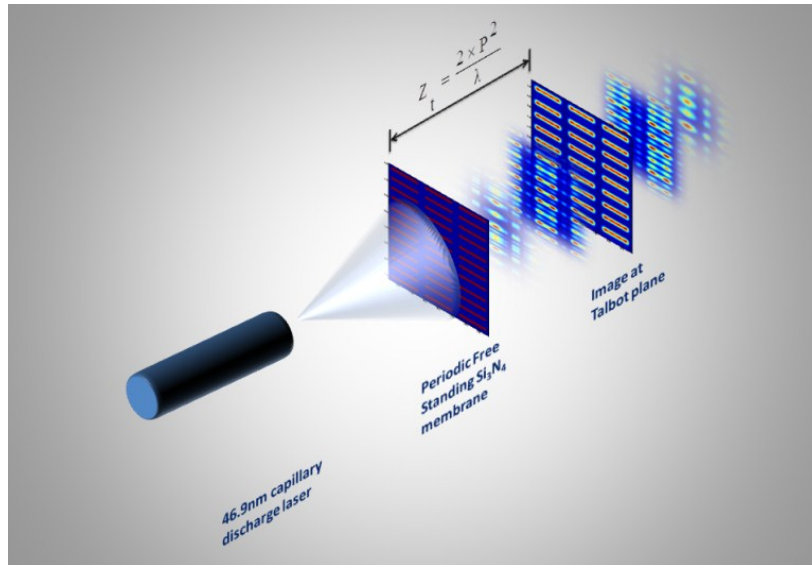


Fig. 2.8 [8] Scheme of Talbot Image set-up

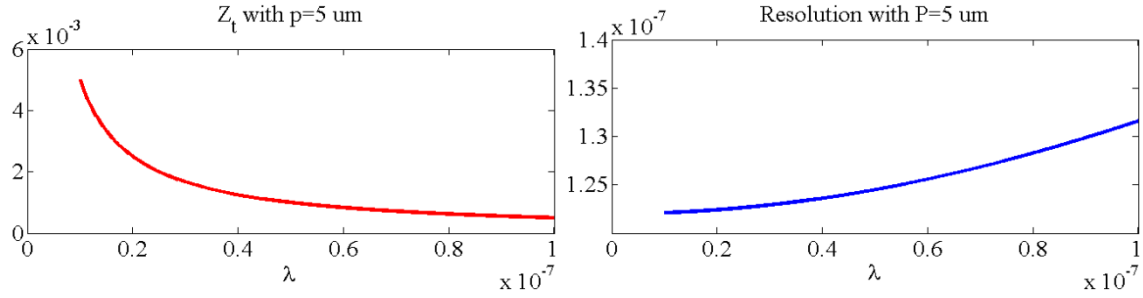


Fig. 2.9 a): Talbot distance and resolution with different period (P)

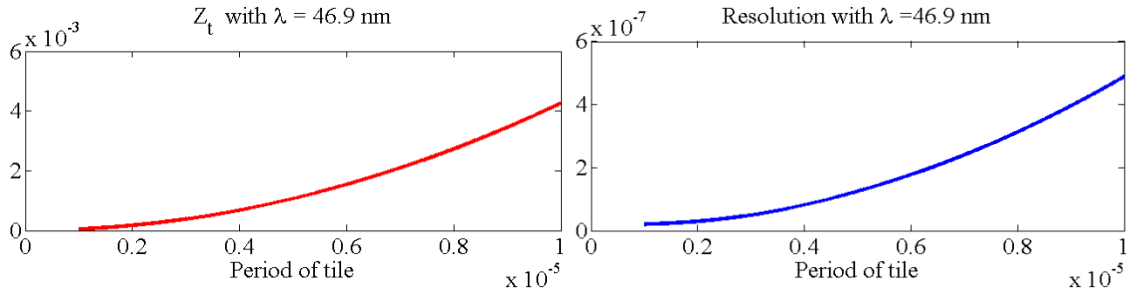


Fig. 2.9 b): Talbot distance and resolution with different wavelength ( $\lambda$ )

The depth of focus (or depth of field) is another important parameter to the system. It was defined in chapter 1 and can be expressed as:

$$DOF = \frac{2 \times \lambda}{NA^2} \tag{2-10}$$

As has been discussed before, the higher numerical aperture will lead to higher resolution, but it also decreases the depth of focus. This makes the alignment of the sample more critical. The resolution and repeatability of the experiment set-up has to be smaller than the DOF in order to make the experiment repeatable.

The Talbot lithography technique can only print periodic patterns. Other functional patterns like line-defect waveguide (shown in figure 2.10) in photonic crystal slabs<sup>[9]</sup> cannot be printed in this self-imaging mechanism as the defects will be corrected.

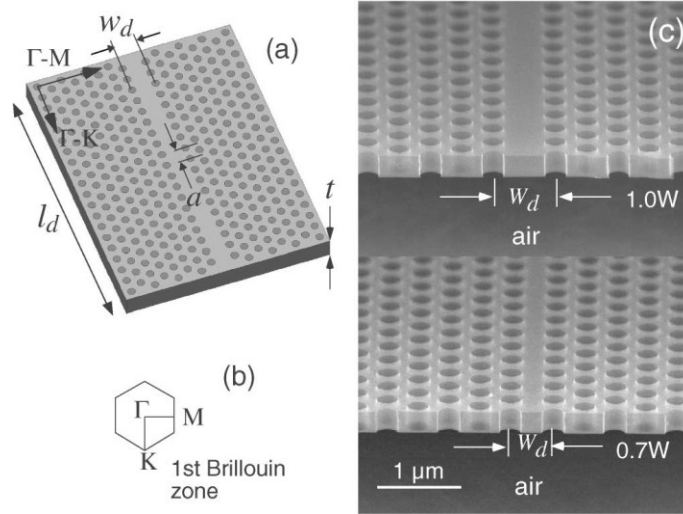


Fig. 2.10<sup>[9]</sup> Line defect waveguide

## 2.4 SIMULATION OF TALBOT IMAGING USING FRESNEL DIFFRACTION

A Matlab code (listed in Appendix I) was developed to calculate the light intensity distribution as a function of the propagation distance  $z$  after the periodic mask when illuminated by a coherent beam. The calculation is based on a fast Fourier transform of the pattern on the mask ( $U(x, y)$ ) and the kernel ( $H(x, y)$ ), and then multiply them in frequency domain. Finally we do the inverse Fourier transform to get the intensity distribution on image plane. The flow chart of the code is shown in figure 2.11.

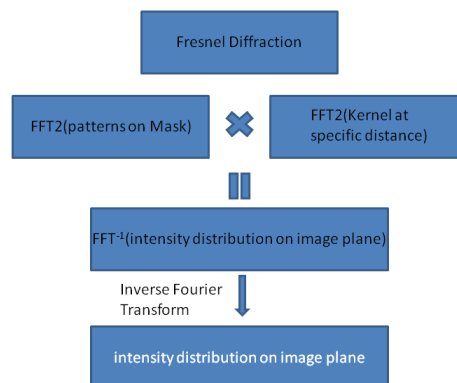


Fig. 2.11 Flow chart of the Matlab code

This code accurately predicted the defect-free character of the Talbot imaging. Simulation results for a defective mask are shown in figure 2.12. Figure 2.12 left is a defective mask where there is one missing bridge in each cell. However, the calculation predicts that this defective mask produces a defect-free image in the first Talbot plane, shown in figure 2.12 right.

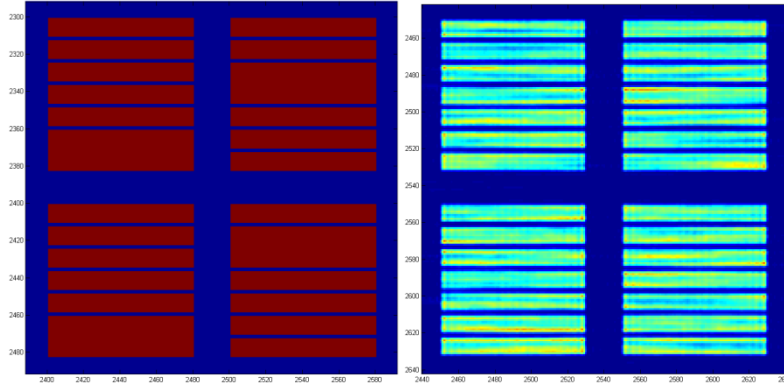


Fig. 2.12: Simulation of defective mask and light intensity distribution at Talbot plane.

## 2.5 MASK DESIGN AND FABRICATION PROCESS

### 2.5.1 Mask design

The Talbot masks in this work have binary transmission. We selected silicon nitride and silicon membranes to define the masks. We designed two kinds of masks. One type of masks was a silicon nitride free-standing mask, where the transparent regions are openings in silicon nitride membrane and the absorber is 50nm silicon nitride together with resist (around 100nm thick) on top; the other kind is a silicon membrane semi-transparent mask which has more than 37.7% transmission on top of which the opaque regions were defined in 60nm HSQ e-beam resist by

electron beam lithography. The geometry of these two kinds of masks is shown in figure 2.13 and the parameters of the mask pattern are shown in Table 2.1.

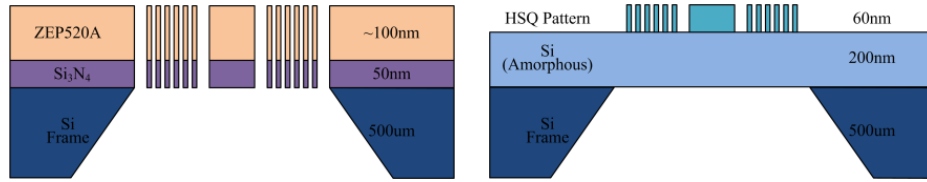


Fig. 2.13 Scheme for two kinds of mask fabricated

Table 2.1 Chart of masks designed

Substrate of the masks	Mask number	Cell period	In cell feature	
			Period	Dimension
Silicon nitride based free-standing masks	# 1	5 um	1.2 μm	φ 300 nm holes
	# 2	5 um	1.2 μm	300 nm gratings
	# 3	5 um	600 nm	100 nm gratings
	# 4	5 um	400 nm	100 nm gratings
Silicon based semitransparent masks	# 5	5 um	Elbows (550nm/700nm line/space)	
	# 6	5 um	Lines (500nm/500nm line/space)	

What remains unknown is the response of the photoresist under different exposure dose because the patterns profiles after being developed are the convolution between the light intensity distribution and the response curve of the photoresist. As shown in figure 2.14, different photoresist will give different response to the same exposure and the FWHM will be also different.

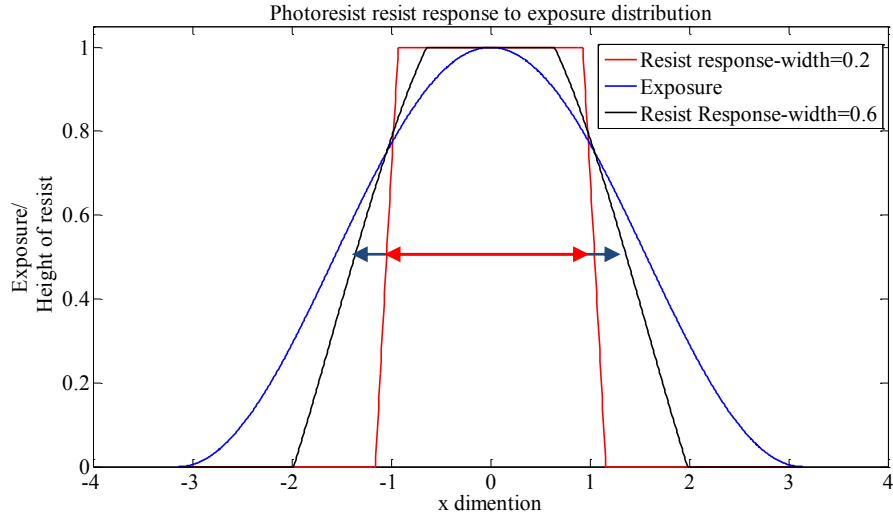


Fig. 2.14 Simulation of pattern profile generated by resists with different response curve at the same exposure dose

The masks were fabricated in Brookhaven National Laboratory. Original patterns were generated by e-beam writer JEOL 6300. Silicon nitride membrane Free-standing mask was etched through by reactive ion etching (RIE) machine TRION. Detailed fabrication process will be presented in next sections. Silicon membrane mask, on the other hand, only needs the cured 60nm HSQ pattern on top of silicon membrane substrate.

To fabricate the masks, membranes with thickness in hundreds of nanometers were chosen for higher efficiency and contrast. The contrast is defined as the ratio between transmittance of the transparent section and the opaque section of the mask. The higher contrast would enhance the feasibility of lithography process. The efficiency on the other hand is the total transmittance of the mask. For the masks used in this work, the contrast and efficiency are shown in table 2.2 below.

Table 2.2 calibration for the contrast and efficiency of the mask

	Contrast	Efficiency
Silicon mask with 60nm HSQ	26.2	37.7%
Silicon Nitride mask (Free-standing)	$>10^5$	100%

From figure 2.13 and table 2.2 we can tell, a thin layer of photoresist (below 100nm) or  $\text{Si}_3\text{N}_4$  membrane (50nm) is enough for a high contrast mask. This means smaller features (sub 100nm) which can only be written in thin film of resist offers sufficient contrast for lithography process. This makes the mask fabrication process easier as it does not require metallization which will introduce unwanted distortion to the structure modifying the topology of the mask.

### 2.5.2 Patterns generated by Jeol 6300

Figure 2.15 is a picture of the Jeol6300 tool<sup>[10]</sup>. The accelerating voltage can be selected from 25kV, 50kV up to 100kV. The electron beam spot can be defined as small as 2nm in mode 3 and 0.125nm in mode 6 (different sets of lenses and apertures are used in different modes). The writing field for mode 3 is 1mm and the one for mode 6 is 62.5  $\mu\text{m}$ . However, the system we utilized can write patterns as large as 200mm because it has a moving stage controlled by laser interferometer with a resolution smaller than 0.6 nm.



Fig. 2.15: E-beam writer: Jeol 6300<sup>[10]</sup>

For free standing silicon nitride masks, ZEP 520A which has higher sensitivity and higher dry etch resistance is used. The spin curve of ZEP 520A for different concentration is

shown in figure 2.16<sup>[11]</sup>. A 50nm thick Si<sub>3</sub>N<sub>4</sub> membrane is used as substrate. In this case, the backside scattering effect can be neglected because most of the electrons injected through the photoresist will also pass through the membrane without scattering back. Higher dose of electrons can be applied without concerning about overexposure. As has been discussed before, our goal is to fabricate free standing masks, which means the layer of resist needs to be high enough to survive after dry etching process. The etching rate of ZEP 520A is smaller than 8nm/s with certain etch parameters (discuss in detail in the next section). While on the other hand, in the same etching parameters, the etch rate of Si<sub>3</sub>N<sub>4</sub> is 1.2nm/s. For 50nm Si<sub>3</sub>N<sub>4</sub>, 350nm ZEP 520A is enough to make a free-standing mask.

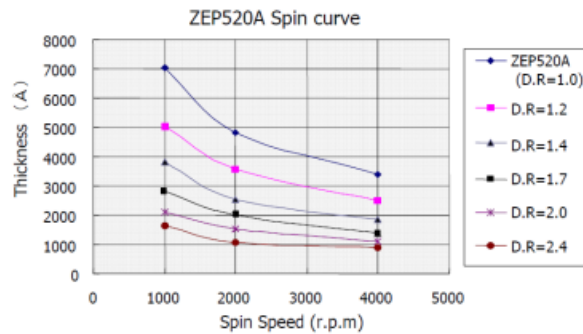


Fig. 2.16 Spin curve of ZEP520A<sup>[11]</sup>

The reactive ion etching (RIE) chamber was first cleaned by O<sub>2</sub> plasma for 10 minutes to get rid of reactive gas residue left by the former user. A 50 nm Silicon Nitride membrane is then cleaned by O<sub>2</sub> plasma for 1 minute. The pressure of the chamber is set to be 100mTorr when CF<sub>4</sub> flows at 5 SCCM (standard cubic centimeter per minute) and O<sub>2</sub> flows at 50 SCCM. The RIE power is set to be 250 W. This process increased the surface roughness of the Silicon Nitride membrane so that the adhesion between the membrane's surface and the e-beam resist is enhanced.

Then, pure ZEP 520A is spin coated onto the membrane at 6000 rpm to give a 350 nm resist film on top. Typically, an e-spacer which is a conductive layer is used in the e-beam lithography. In our case, however, an e-spacer is unnecessary because the charges would rather passing through the 50 nm membrane than accumulate on the surface. The prepared membrane was then clamped on the cassette designed for 3mm trench. Exposures with different doses have been tested to calibrate the optimal dose for certain pattern.  $4000 \mu\text{C}/\text{cm}^2$  is the optimal dose for 500 nm gratings and 300 nm holes. Mode 3 and 500 pA current accelerated to 100 kV were used during the e-beam exposure. The aperture set used in this process is number 5.

After being exposed by the Jeol 6300, the membrane is put on top of a hot plate with 180 °C for 3 minutes to amplify the chemical reaction between the electrons and the e-beam resist. Patterns were created after being developed in Amyl-acetate for 90 seconds and it should be soaked in IPA for 90 seconds before being taken out. The process flow is concluded as the following:

- Clean the chamber for RIE with  $\text{O}_2$  plasma for 10 minutes;
- Clean the  $\text{Si}_3\text{N}_4$  membrane in  $\text{O}_2$  plasma for 1 minute;
- Spin coat pure ZEP520A at 6000 rpm on to 50nm  $\text{Si}_3\text{N}_4$  membrane;
- Expose in Jeol 6300 for  $4000 \mu\text{C}/\text{cm}^2$  at 500 pA in mode 3;
- Post-bake the membrane at 180 °C for 3 minutes;
- Develop at Amyl-acetate for 90s and soak in IPA for 90s.

### 2.5.3 Etch process for free-standing mask

For free standing mask (scheme shown in figure 2.13 left), the patterns created by e-beam lithography are used as a sacrificial mask in the etching process to open the silicon nitride.

Typically, the resist does not serve as a sacrificial mask. Usually, a layer of metal, like Cr, is used as a sacrificial mask in RIE. However, 350nm ZEP520A is resistant enough for our purpose due to the thickness of the thin membrane and high dry etch resistance of ZEP. The height and the etching rate of the resist and membrane have been calibrated in previous tests. Eliminating the metal sacrificial mask makes the fabrication process much more stable, repeatable and easier. It makes advantages of the high absorption coefficient of 46.9nm so that only 50 nm  $\text{Si}_3\text{N}_4$  can absorb more than 98% of the light exposed on.

RIE chamber is firstly cleaned with  $\text{O}_2$  plasma for 5 minutes in order to make sure a stable etching process in the following. Then  $\text{CF}_4$  (40 SCCM) and  $\text{O}_2$  (10 SCCM) were injected to etched  $\text{Si}_3\text{N}_4$ . Pressure is set to be 50 mTorr and RIE power is 150 W. The mask was processed for 50 s in such parameters in order to make sure the opening. One of the fabricated free-standing masks is shown in figure 2.17.

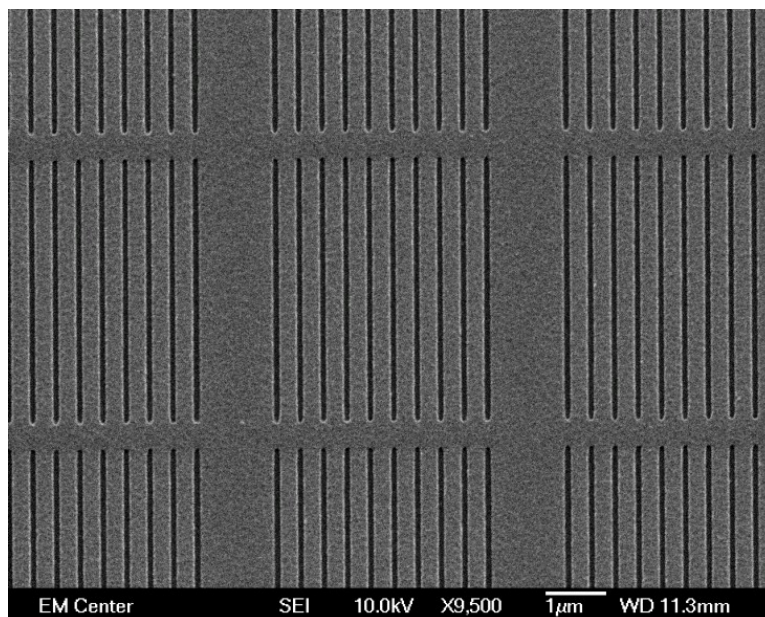


Fig. 2.17: Example of fabricated mask

Another kind of mask is fabricated on a 200 nm thick silicon membrane. The geometry of this kind of mask is shown in figure 2.13 right. The absorbing regions were defined in a layer 60 nm thick of photoresist HSQ. For this structure the fabrication process is easier and the efficiency of the mask is 37.7%.

RIE chamber is firstly cleaned by O<sub>2</sub> plasma for 10 minutes. The surface of silicon membrane is also cleaned by O<sub>2</sub> plasma. The pressure of the RIE chamber is set to be 100 mTorr with oxygen flowing at 50 SCCM. The power of RIE is set at 50 W. After the surface of silicon membrane is cleaned by O<sub>2</sub> plasma, 60 nm thick 4% HSQ (H<sub>8</sub>Si<sub>8</sub>O<sub>12</sub>) is spin coated on. An e-spacer is spin coated on this time. Prepared silicon membrane is then exposed by electron beam. Mode 3 and 10 nA current is used during the e-beam lithography. Dose for these masks is 4000 μC/cm<sup>2</sup>. The developer used is a mixture between 1wt % NaOH and 4wt % NaCL for 3 minutes. One of the fabricated masks based on silicon membrane is shown in figure 2.18.

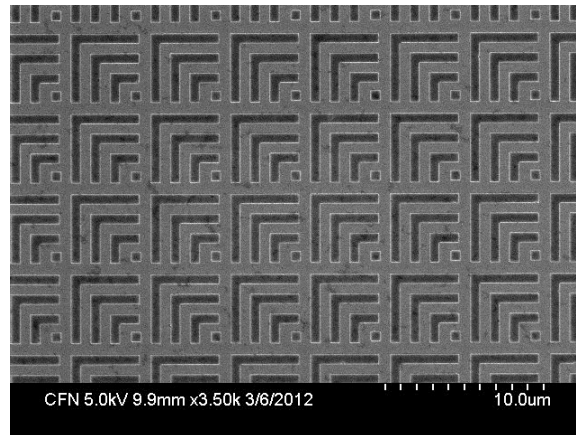


Fig. 2.18: Fabricated mask based on silicon membrane

#### 2.5.4 Results of mask fabrication

Figure 2.19 a)-d). are scanning electron micrographs of a section of a mask having a total area 0.5mm×0.5mm and composed of 10000 unit cells. The unit cell is 5 μm × 5 μm. Four

different masks have different motifs on each membrane. In figure 2.19 a), the tile is composed by 4 slits which are 500 nm wide and they are separated by 700 nm. In figure 2.19b), the tile is composed by 7 slits which are 500nm wide and they are separated by 100nm. In figure 2.19 c), the tile is composed by 3×3 array of holes which are 360 nm in diameter and they are separated by 1200 nm. In figure 2.19 d), the tile is composed by 100 nm slits separated by 300 nm space. During the etching process, the mask shown in figure 2.19 b) was over etched making some 100 nm wide silicon nitride bridges collapsed (highlighted with red circles).

HSQ masks supported on silicon membranes were also designed and fabricated shown in figure 2.19 e)-f). 40, 000 units of this motif covering 1 mm × 1 mm area were written to form single pattern on the mask. The period of each motif on both masks is 5 μm. In figure 2.19 e), the tiles are composed of elbows whose linewidth is 550 nm. The space between each elbow lines is 700 nm. In figure 2.19 f), the motif is composed of periodic lines and isolated lines whose linewidth and space are both 500 nm. The scheme of these silicon membrane based HSQ masks is shown in figure 2.13 (right).

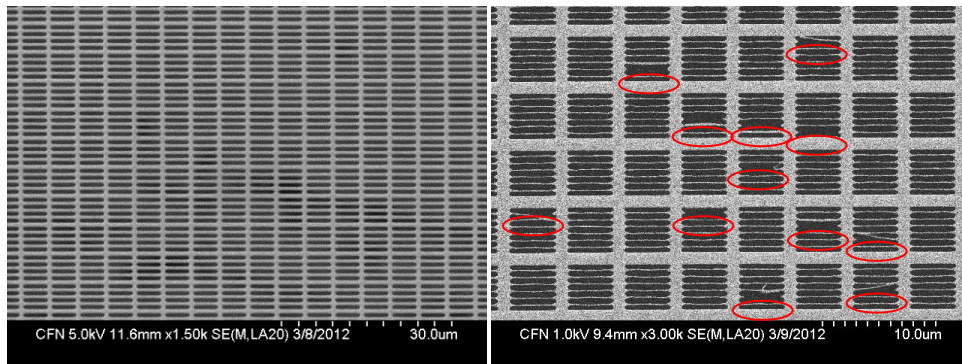


Fig. 2.19 a): P1.2umW500nm

Fig. 2.19 b): P600nmW100nm

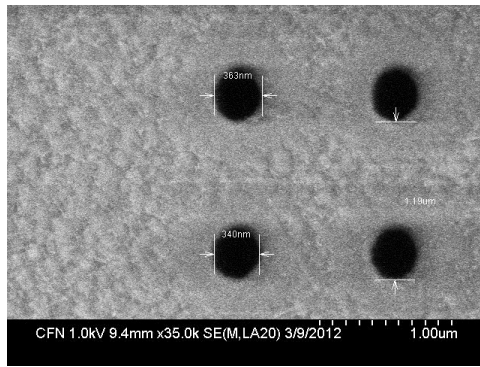


Fig. 2.19 c): P1.2umD300nm

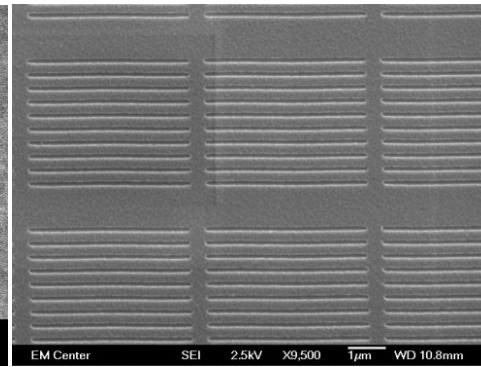


Fig. 2.19 d): P400nmW100nm

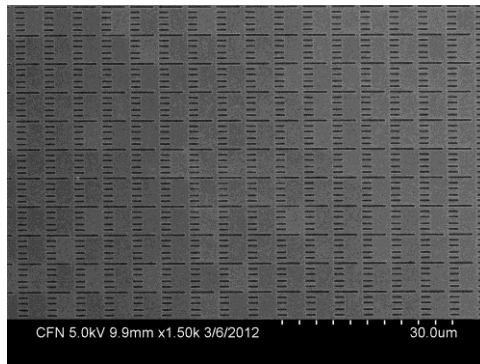


Fig. 2.19 e): Silicon membrane based lines

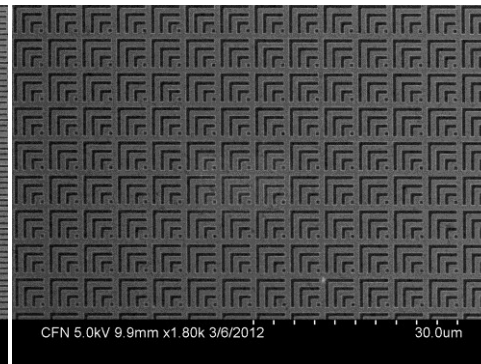


Fig. 2.19 f): Silicon membrane based elbows

In order to make it easier for the reconstruction with Talbot imaging, 9 mask patterns were written on the same membrane with slightly different cell periods (shown in figure 2.20). 50 nm period variance and 200  $\mu\text{m}$  space between adjacent mask patterns make the reconstruction much faster because the working distance is no longer a single depth of focus, i.e. 500 nm, but a continuous long region, i.e. 10  $\mu\text{m}$ .

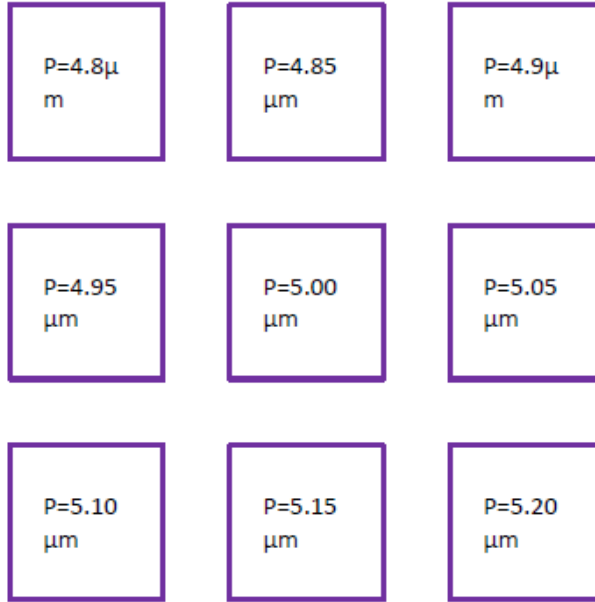


Fig. 2.20 Assemble 9 masks on the same membrane

## 2.6 REFERENCES

- [1] ROCCA, JJ; SHLYAPTSEV, V; TOMASEL, FG; et al. 'DEMONSTRATION OF A DISCHARGE PUMPED TABLE-TOP SOFT-X-RAY LASER', PHYSICAL REVIEW LETTERS, Volume: 73 Issue: 16 Pages: 2192-2195, Published: OCT 17 1994.
- [2] Urbanski, L, Rocca, JJ , 'Spectral linewidth of a Ne-like Ar capillary discharge soft-x-ray laser and its dependence on amplification beyond gain saturation', PHYSICAL REVIEW A Volume: 85 Issue: 3, 2012.
- [3] Y. Liu, M. Seminario, D. T. Attwood et al. , 'Achievement of essentially full spatial coherence in a high-average-power soft-x-ray laser', Physical Review A, Volume 63, 2001.
- [4] Introduction to Fourier Optics 2<sup>nd</sup>, J. Goodman, p67
- [5] Christel Zanke, Minghao Qi, and Henry I. Smithb, 'Large-area patterning for photonic crystals via coherent diffraction lithography', JVST B, 22(6), 2004
- [6] A. Isoyan, F. Jiang, M. C. Marconi, J. Vac. Sci. Technol. B 27, 2931 (2009).
- [7] Urbanski, L, Stein, A., Rocca, J.J., Menoni, C.S., Marconi, M. C. , 'Defect Tolerant EUV Nanoscale Printing'. Optics Letters, 2012, 37
- [8] W. Li et. al, 'Fabrication of periodic structures using coherent Talbot lithography in a table top system', JVSTB, to be published.

- [9] M. Notomi, K. Yamada, A. Shinya, J. Takahashi, C. Takahashi, and I. Yokohama, 'Extremely Large Group-Velocity Dispersion of Line-Defect Waveguides in Photonic Crystal Slabs', Physical review letters, Volume 87, Number 25, 2001.
- [10] [www.jeol.com/Product/Semiconductorequipment/ElectronBeamlithography](http://www.jeol.com/Product/Semiconductorequipment/ElectronBeamlithography)
- [11] [http://www.zeon.co.jp/business\\_e/enterprise/imagelec/imagelec.html](http://www.zeon.co.jp/business_e/enterprise/imagelec/imagelec.html)

## CHAPTER 3 METALLIZATION PROCESS

The nano-patterns in photoresist were transferred faithfully to the metal substrate by chemically assist ion beam etching system which was rebuilt and calibrated as part of this work. The mechanism, operation, advantages and the performance of this machine will be discussed in this chapter.

### 3.1 CHEMICALLY ASSIST ION BEAM ETCHING SYSTEM (CAIBE)

#### 3.1.1 *Mechanism of CAIBE*

Ion beam etching (IBE) is a technique that uses a directional ion beam to sputter or ablate the sample. The process of ablation is initiated by physical bombardment between individual energetic ions from the charged particle beam and the surface of target. CAIBE is an extension from IBE so that the physical ablation effect is enhanced by chemical reaction. The results shown in the following sections only utilized the IBE function which is more stable and it is easier to control the etching rate. The scheme of this system is shown in figure 3.1.

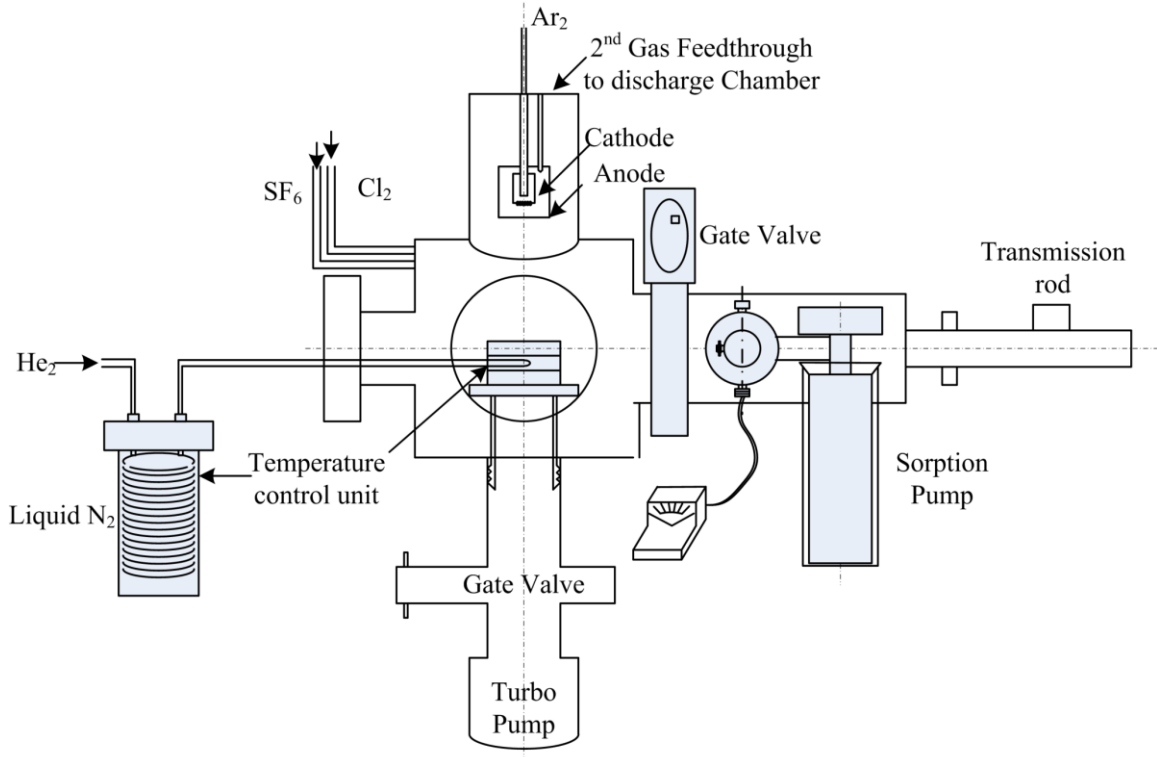


Fig 3.1 CAIBE scheme

The plasma source of the IBE is a Hollow Cathode which offers significant advantages over the heated filament cathode normally used in an ion beam source. Hollow cathode <sup>[1]</sup> has a much longer life-time and is able to offer a much cleaner plasma without possible sputtering contamination from heated filament (usually is a metal). The details of this hollow cathode assembly are shown in figure 3.2. Argon gas is injected through the hollow cathode tip and the plasma discharge is initiated by a heater current which heats the tip up to 1000 °C. In the mean time, a 350-500 V voltage is applied to the keeper electrodes which draw away the additional electrons from the hollow cathode plasma so that the ion source discharge is initiated and sustained. A potential difference exists between a baffle which isolates the cathode discharge assembly from the source discharge assembly. With the optimized potential difference across the baffle, electrons are accelerated into an energy range where the ionization cross section is almost maximized. When the electrons are heading towards anode, magnetic field from the poles forces

the electrons to follow a longer path. Lengthy electron path increases the probability of ionization collisions with the Argon gas atoms in the source chamber. After all, a sustainable, stable and energetic ion beam is generated when some of the ions in the discharge reached to the grids assembly which focused and accelerated the ions towards the target underneath.

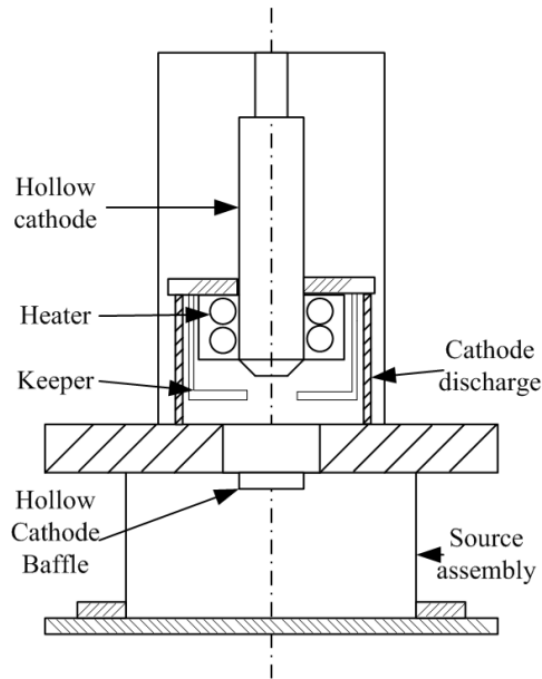


Fig. 3.2 Ion beam source based on Hollow cathode assembly

### 3.1.2 Operation of CAIBE

IBE system needs to be run in high vacuum. Before the argon flows into the system, it needs to be pumped down to  $10^{-6}$  Torr. When 10 SCCM Argon are being injected to the system, the system requires a pumping speed large enough to maintain a vacuum under  $10^{-4}$  Torr. After the system has been pumped down to  $10^{-6}$ , the argon supply line needs to be purged by 3 SCCM argon flows which are controlled accurately by a mass flow controller for at least 3 hours. With a comparative pure Argon circumstance, an increasing current is applied to the heater around the hollow cathode tip where argon flows through at 2.5 SCCM. After the heater current is increased

to 7.25A for less than 2 minutes, a discharge should be built. If not, the Argon flow rate should be enhanced up to 6 SCCM until a discharge is well built. The heater current then drops automatically to 3.75A. However, in different conditions, the heater current can vary from 3.75A to 4.5A or even higher. In this case, Argon flow should be changed accordingly so that the heater current is stable. This is very important to enhance stability of the ions and the life-time of the hollow cathode. To decrease the amount of oxygen inside the system when the cathode tip is heated, samples are loaded at least 15 minutes before the power supply is turned on. In addition, the load-lock gate is opened 15 minute after the heater is cooled by Argon flow. The power supply has a build-in memory in which the program '0' stored the optimized voltage & current set-up for Ar plasma. When the discharge is built, the discharge voltage decreases below 100 V and the discharge current should be around the set up value. After few minutes, the plasma is steady inside the discharge chamber. Once the accelerating voltage is applied by pressing 'start the beam', the ion beam is extracted to the etching chamber and the etching process is initiated.

The samples are clamped to the holder mounted onto the transmission rod. At the beginning of the process, it is located on the low vacuum side of the system. With a closed gate-valve, the load-lock chamber is pumped down to 50 mTorr by a sorption pump. Then the gate valve can be opened and the sample is inserted to the temperature control unit which also has two spring screws to lock the holder tightly. The holder can then be released from the transmission rod by rotating 90 degree. The gate-valve should be closed after the transmission rod is moved back to the load-lock chamber. Before the sample is etched by the Ar plasma, a shelter blocks the ion beam for 1 minute to stabilize the ion beam. The operation flow can be concluded as following:

- Pump the main vacuum to  $10^{-6}$  Torr;
- Purge the Argon gas line with 3 SCCM flow for 3 hours. (During this time the vacuum should be under  $10^{-4}$ );
- Clamp the sample to the copper holder and mount them together to transmission rod;
- Pump the load-lock chamber to 50 Microns;
- Open the gate-valve all the way;
- Insert the transmission rod gently to the main chamber and lock it to the temperature control unit;
- Release the transmission rod and move it back to the load-lock chamber;
- Shut down the gate valve and leave the main chamber pumping for 10 more minutes to eliminate the oxygen introduced from the load-lock chamber;
- Set the Argon flow controller at 2.5 SCCM and then open the power supply by recalling program '0';
- Wait the heater current going up to 7.25A and 2 minutes later the discharge should be built;
- If not, increase the argon flow until the discharge is built but the argon flow should not exceed 6 SCCM;
- After the heater current decreasing to 3.75A and discharge voltage and current being stable, start the beam with the shelter blocking it.

## 3.2 TEMPERATURE CONTROL AND THICKNESS MONITOR SYSTEM

### 3.2.1 Temperature control unit

Stabilizing the temperature of the sample is fundamental in order to stabilize the etching rate and obtain repetitive results. In this work a temperature stabilization system (shown in figure 3.3) was built to take away the heat generated by massive ion bombardment. The temperature is stabilized by circulating cooled He through the base of the sample holder. The helium is cooled by flowing it through a copper coil immersed in liquid nitrogen. Cooled helium flows inside an empty copper cavity on top of which the sample holder is locked tightly by a spring loaded set-screw. A thermo couple is placed inside the cavity to detect the temperature. The whole set is all made of copper which has a high heat conductivity. All the experiment is carried out at the temperature of  $0\text{ }^{\circ}\text{C} \pm 3\text{ }^{\circ}\text{C}$ .

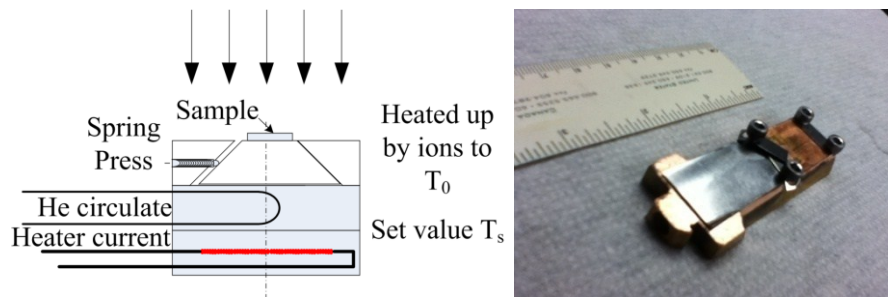


Fig. 3.3 Helium cooling unit on left and sample holder on right

### 3.2.2 Thickness monitor

A thickness monitor is designed to locate close to the sample holder (shown in figure 3.4). The thickness monitor used in our set-up is based on a 6 MHz quartz monitor crystals (QMC) coated by silver made from INFICON [2]. The controller accompany with QMC shows

the etching rate and etching height simultaneously. A portion of ions are used to indicate the etching rate.

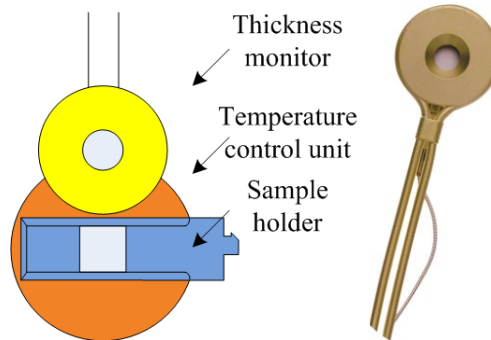


Fig. 3.4 Thickness monitor based on QMC

### 3.3 CALIBRATED ETCHING RATES AND STABILITY OF THE SYSTEM

After following the process flow and applying helium cooling, the system is able to metalize resist pattern stably in a longer time. In order to check the linearity, stability and repeatability of CAIBE, a simple but trust worthy experiment is designed and carried out. As the scheme shown in figure 3.5, a thin piece of quartz is clamped on top of the target which might be a photoresist spin-coated on or a special metal film thermally evaporated on silicon substrate. The quartz piece only covered and protected part of the target, leaving the other part being exposed by the energetic ion beam. A height difference is hence created and measured by alpha-step.

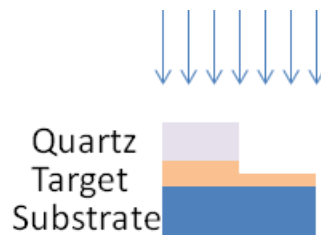


Fig. 3.5 Experiment set-up for etch rate calibration

Etch rate for HSQ, AZPN, gold, Silicon and hard baked HSQ (HB HSQ) are calibrated. The data collected is shown in table 3.1. Besides the data shown in the table, the etch rate for HSQ is the same as for Silicon and the etch rate for AZPN is 37.5% smaller than silicon. Figure 3.6 collects the data in table 3.1 and the linearization.

Table 3.1 a) Etch rate calibration for silicon

Etch time (s)	60	120	180	240	307
Edge height (nm)	19.313	41.667	65.4	81.2	111.5

Table 3.1 b) Etch rate calibrations for HB HSQ

Etch time (s)	60	120	180	240
Edge height (nm)	11.4	22.2	31.05	44.633

Table 3.1 c) Etch rate calibration for gold

Etch time (s)	61	120	180	270
Edge height (nm)	50.3	125.55	197.625	309.217

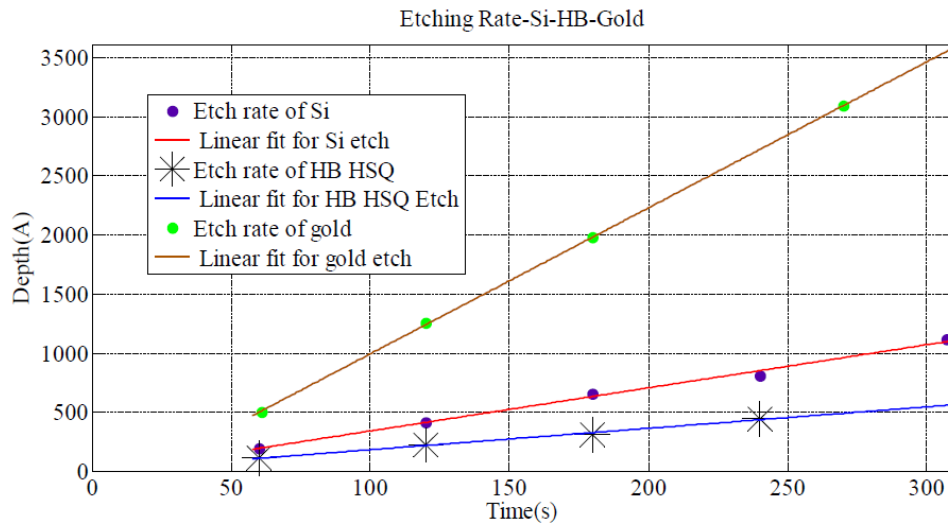


Fig. 3.6 Etch rate for Silicon, HB HSQ and gold

In addition to this, a stability experiment was carried out for gold. HSQ patterns were created on top of gold film by contact lithography. The patterns were then transferred by CAIBE

with the HSQ patterns as masks. Photoresist residue is removed by HF. The results were scanned by Atomic Force Microscope (AFM) which has a better resolution than  $\alpha$ -step. One of the pattern & metallization result is shown in figure 3.7. The remaining data of the etching results are shown in figure 3.8 which indicates the etching error of this system is smaller than 5%.

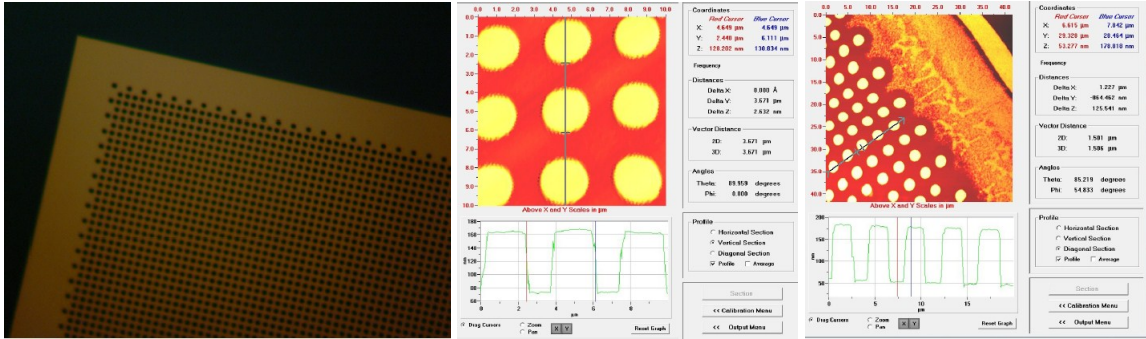


Fig. 3.7 a) Mask

Fig. 3.7 b) HSQ pattern

Fig. 3.7 c) Etched pattern

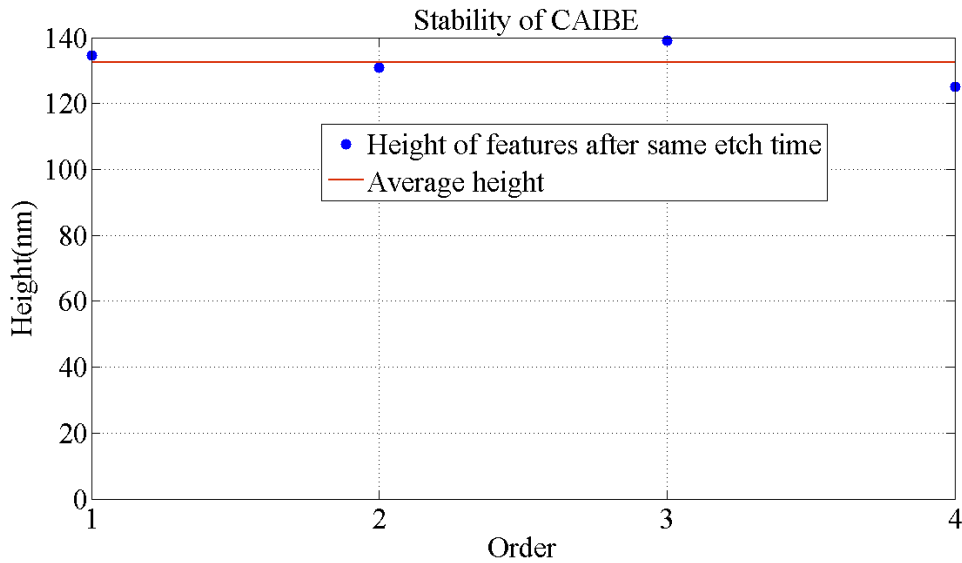


Fig. 3.8 Stability experiment for gold (data is measured by AFM)

### 3.4 REFERENCE

- [1] 'HC-252 Hollow Cathode Manual', ION TECH, inc.,
- [2] <http://www.inficonquartzmonitorcrystals.com/en/index.html>

## CHAPTER 4 RESULTS OF TALBOT IMAGING

In this chapter the preparation of the sample, the experimental results of the Talbot lithography and IBE process are described. This is a complete nanofabrication process based on a novel photolithographic method. Defect free nanopatterns are printed in different photoresist like HSQ, PMMA and AZPN from Talbot mask. They are also used as sacrificial mask in the IBE process subsequently. The fabricated nanopatterns in photoresist and metal substrate are scanned by an Atomic Force Microscope (AFM) or a Scanning Electron Microscope (SEM).

### 4.1 PREPARATIONS OF THE SAMPLES AND THEIR PROCESS PROCEDURES

#### 4.1.1 *Preparation of HSQ sample for free-standing silicon nitride masks*

For the free-standing silicon nitride membrane masks (shown in figure 2.19 a, b, c & d), HSQ was used due to its high resolution and etching resistance. A 5 nm Cr (adhesive layer) and 100 nm Au layer were coated onto silicon wafer accordingly by thermal evaporation. Since HSQ cannot be spin-coated directly onto gold film, to enhance the adhesion between the gold and the HSQ film, trimethoxysilane (3-MPT) is used to create a homogeneous hydroxylation layer on top of gold<sup>[1]</sup>. 3-MPT is self-assembled onto gold substrates via Au-S bond and the scheme for this bond is shown in figure 4.1. To grow this self-assembled monolayer, a gold coated wafer was immersed in 0.02 M 3-MPT solution (Ethanol base) for 1.5 hours. Wafers were then rinsed with ethanol and immersed in 0.1 M HCL solution (DI water base) for another 1.5 hours to stop the self-assemble process and neutralize the ethanol on the surface of gold. 4% HSQ was then spin-coated on top of 3-MPT at 3500 rpm. This 60 nm HSQ film was prebaked at 95 °C for 1 minute before it was mounted in the experiment set up shown in Chapter II section 1. The sample was then exposed by 46.9 nm EUV laser with a calibrated dose (according to the dimension of the patterns on mask). The calibrated doses are shown in table 4.1. 8 minutes post bake at 115 °C is

applied to the exposed sample before it is developed in TMAH (tetramethylammonium hydroxide,  $(\text{CH}_3)_4\text{NOH}$ ) for 5 seconds. The developed sample should be immersed to DI water for 30 seconds after the development to stop the process.

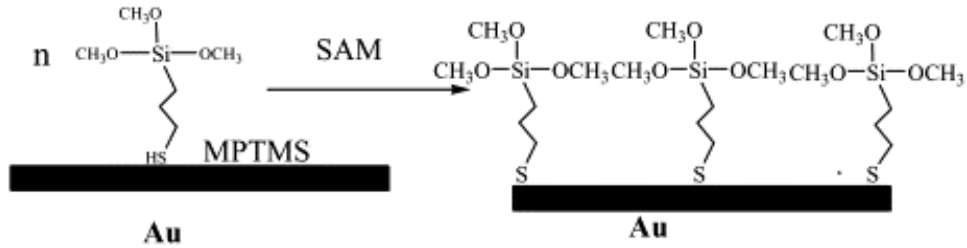


Fig. 4.1: SAM process of 3-MPT on top of gold substrate<sup>[2]</sup>

Table 4.1 Process parameters for different photoresist on different samples

	Mask	Prebake		Dose (shots)	Post bake		Development	
		Time (mins)	Temperature (°C)		Time (mins)	Temperature (°C)	Developer	Time (S)
HSQ on gold (for dots)	Silicon nitride free-standing mask	1	95	270	8	115	TMAH	5
HSQ on gold (for gratings)	Silicon nitride free-standing mask	1	95	50	8	115	TMAH	5
AZPN on gold	Silicon mask	1	120	270	8	105	50% TMAH (water )	45
AZPN on silver	Silicon mask	1	120	270	8	105	50% TMAH (water )	45

#### 4.1.2 Preparation of AZPN samples for silicon membrane masks

For silicon membrane masks (shown in fig. 2.15 e & f), a chemical amplified photoresist AZPN 114 was used. Silicon wafers are first coated by silver or gold. The silver samples were prepared by evaporating 120 nm silver. HDMS (Hexamethyldisilazane) is spin coated onto silver at 3500 rpm. This HDMS layer is to enhance the adhesion between silver and AZPN (10% concentration) which is spin coated subsequently at 3500 rpm leaving a 65 nm AZPN layer afterwards. The photoresist coated sample was prebaked on a hot plate at 120 C for 1 minute before being hooked up to the experiment chamber and exposed by 46.9 nm laser with 270 shots. Exposed sample was then post baked at 105 C for 8 minutes. Finally, the sample was developed by being immersed in 50% TMAH for 45 seconds.

Gold samples for silicon membrane masks needed more steps in the fabrication. A 5 nm Cr was evaporated between silicon wafer and gold film (100 nm). To enhance the adhesion for AZPN 114 to gold, 3 nm Cr and HMDS were coated on top of gold surface accordingly. The exposure process for gold sample and silver sample were identical. The scheme of the gold-HSQ sample for free-standing silicon nitride membrane is shown in figure 4.2 a). The scheme of silver-AZPN sample for silicon membrane masks is shown in figure 4.2 b). The geometry of the Au-AZPN sample is shown in figure 4.2 c).

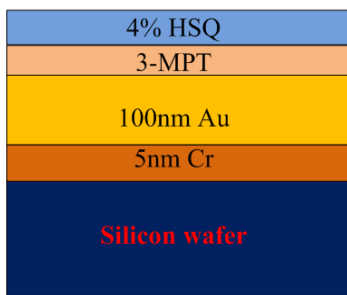


Fig. 4.2 a) HSQ on gold sample

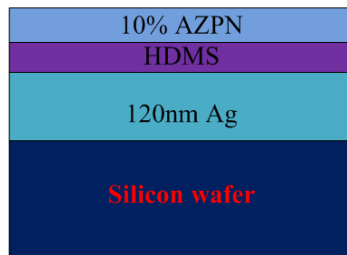


Fig. 4.2 b) AZPN on silver sample

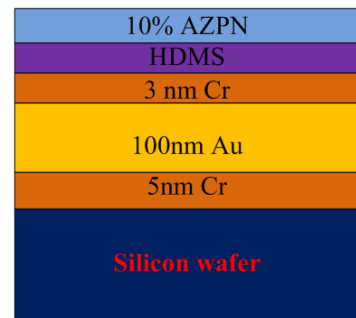


Fig. 4.2 c) AZPN on gold sample

## 4.2 RESULTS OF TALBOT IMAGING

After the samples were prepared, they were exposed and developed following the procedures in Table 4.1. The results are shown in figure 4.3. Figure 4.3a are the SEM and AFM scan for HSQ pattern (300 nm dots with 1.2  $\mu\text{m}$  periodicity) on gold substrate. The mask used in the Talbot imaging was a silicon nitride free-standing mask (shown in figure 2.15 c). Figure 4.3 b is the SEM scan for 500 nm gratings separated by 100 nm and it is a HSQ pattern which is duplicated from a defective silicon nitride free-standing mask (shown in figure 2.15 b). Figure 4.3 c is the AFM scan for AZPN pattern which is composed of elbows with 550/700 nm line and space. The silicon membrane mask shown in figure 2.15 f is used for elbows. Figure 4.3 d is an AFM scan for AZPN pattern which is composed of periodic and isolated lines with 500 nm linewidth and spaces (the mask was shown in 2.15 e). The comparison between the masks (shown in figure 2.15) and the Talbot printing results shown in figure 4.3 proves that this EUV Talbot lithography is able to reconstruct the periodic features from the mask accurately. Figure 4.3 b also proves again that this work is a defect-tolerant technique.

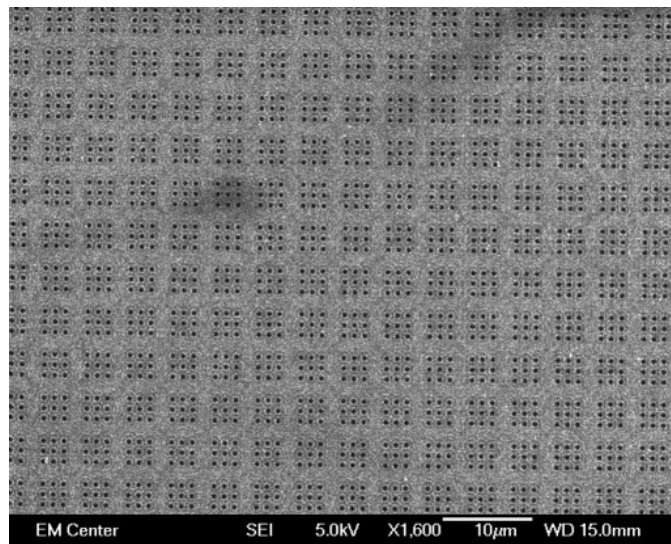


Fig. 4.3 a: 320 nm nano-dots in HSQ (SEM and AFM scan inset)

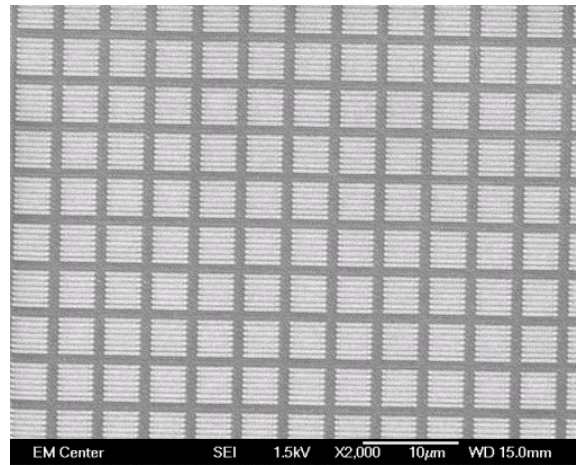


Fig. 4.3 b: HSQ pattern with 500 nm gratings separated by 100 nm (SEM scan)

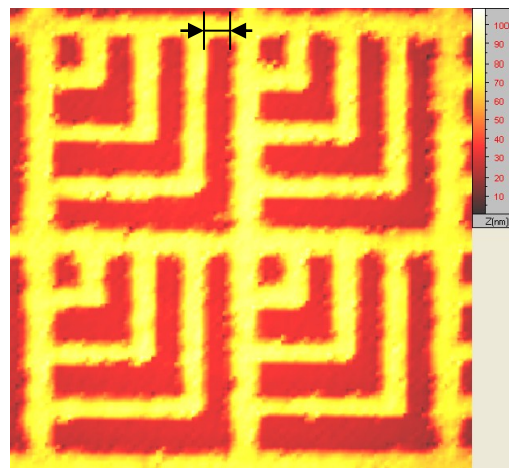


Fig. 4.3 c: AZPN patterns (elbows) on top of gold, 500 nm linewidth.

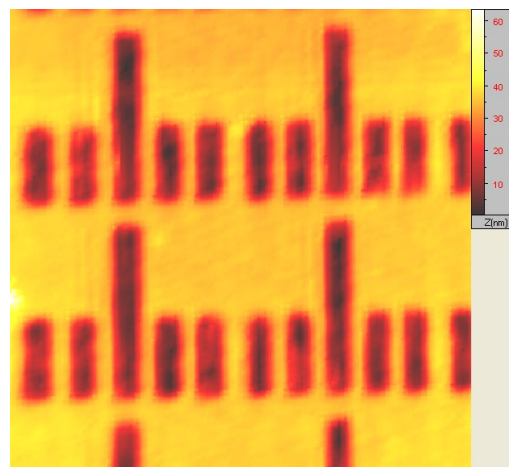


Fig. 4.3 d: AZPN patterns (lines) on top of silver, 500 nm linewidth.

### 4.3 METALLIZATION RESULTS

The photoresist patterns were then used as sacrificial masks for IBE process. The results after the etching process are shown in figure 4.4. Figure 4.4a is 500 nm gratings in gold transferred from the HSQ pattern (shown in figure 4.3 b). They are separated by 100 nm between each grating. Figure 4.4 b are elbows with 550/700 nm line and space that was transferred from AZPN pattern (shown in figure 4.3 c). Figure 4.4c is the periodic and isolated lines with 500 nm line and space in silver film. The AZPN patterns used as sacrificial mask were shown in figure 4.3 d. Figure 4.4 c are 300 nm nano-dots in gold which was transferred from HSQ patterns shown in figure 4.3 a. Compared with figure 4.3, which shows the photoresist patterns (used as sacrificial mask), figure 4.4 demonstrated that IBE process in this work is able to transfer patterns anisotropically and faithfully.

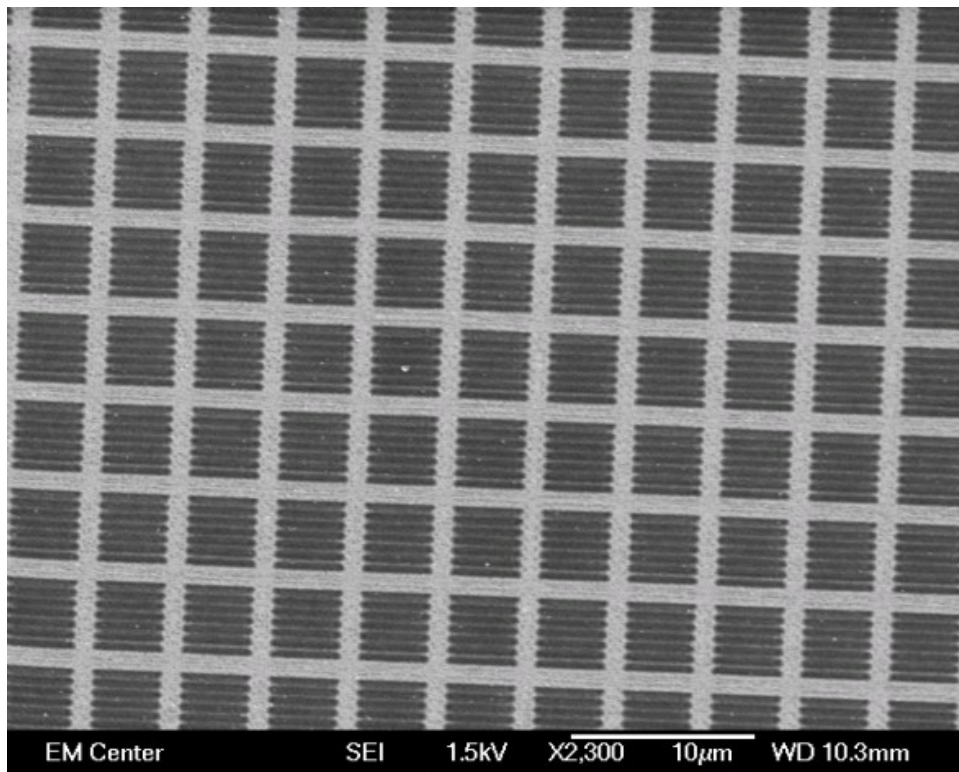


Fig. 4.4 a: 500 nm gratings separated by 100 nm (etched to 100 nm gold)

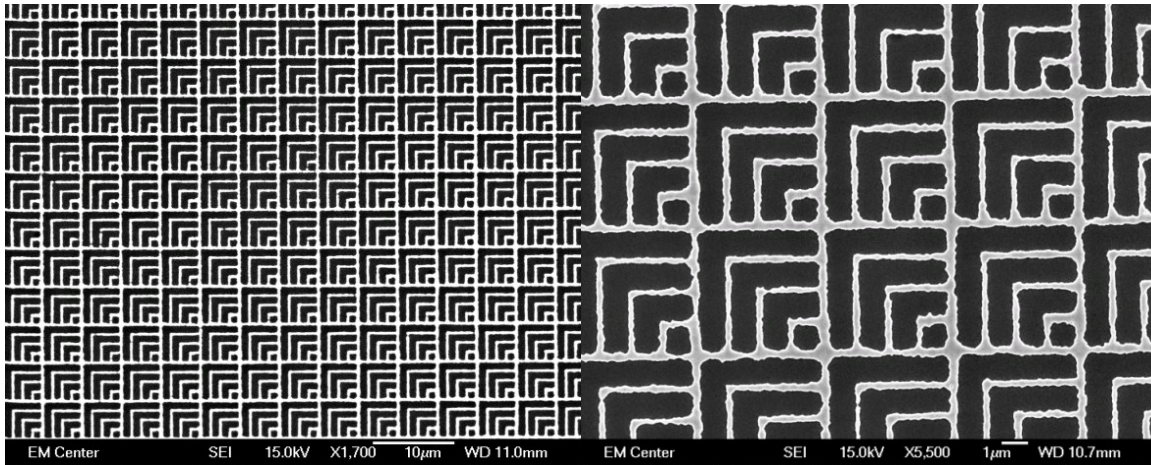


Fig. 4.4 b: Elbows 550/700 nm line and space (etched to 100 nm gold)

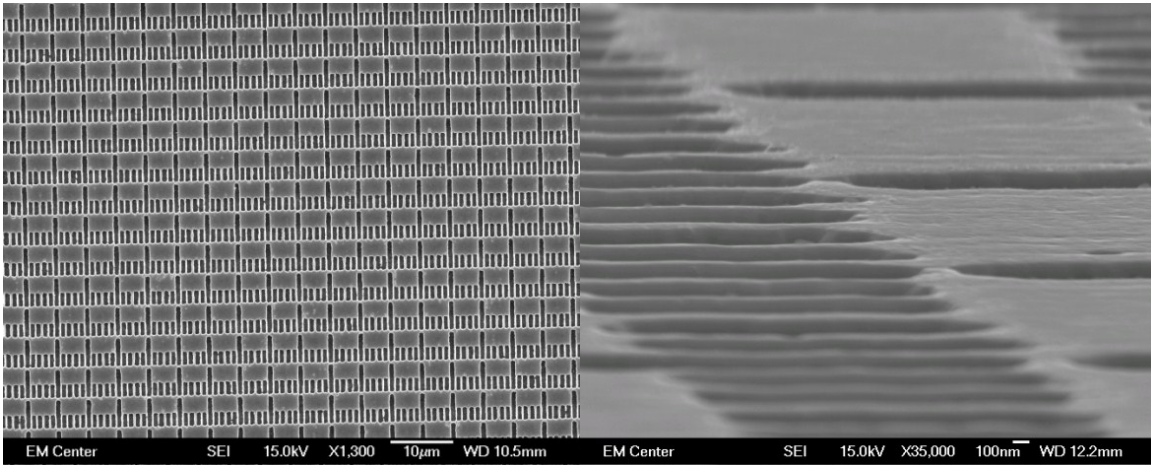


Fig. 4.4 c: Periodic and isolated lines with 500 nm line and space fabricated in 120nm silver; right figure is a tiled image

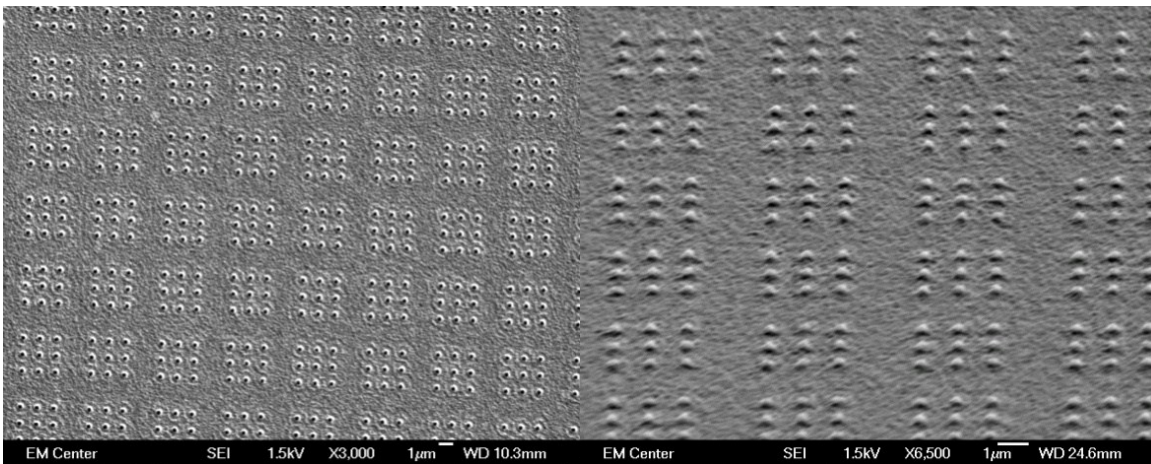


Fig. 4.4 d: 300 nm nano-dots etched to gold; right figure is a tilted image

#### 4.4 ANALYSIS OF THE RESULTS

In this section, the results for Talbot imaging and IBE process are analyzed and compared to the patterns on original mask. A comparison is shown in table 4.2. The statistics of each pattern are summarized from figure 4.5 to 4.7. Figure 4.5 shows the data for the line width of elbows fabricated in AZPN (figure 4.5 a) and gold (figure 4.5 b). Figure 4.6 show the data for linewidth of periodic & isolated lines in AZPN (figure 4.6 a) and silver (figure 4.6 b). Figure 4.7 shows the data for diameters of pillars in HSQ (figure 4.7 a) and gold (figure 4.7 b).

Table 4.2: Comparison between patterns on masks, photoresist and metal

Patterns:	Patterns on Mask		Patterns on photoresist		Metalized patterns	
	Critical dimension (CD)	Figure #	Average CD (nm)	Figure #	Average CD (nm)	Figure #
Elbows	550 nm	2.15 f	570	4.3 c	580	4.4 b
Periodic & isolated Lines	500	2.15 e	500	4.3 d	566	4.4 c
Pillars	360	2.15 c	355	4.3 a	297	4.4 d

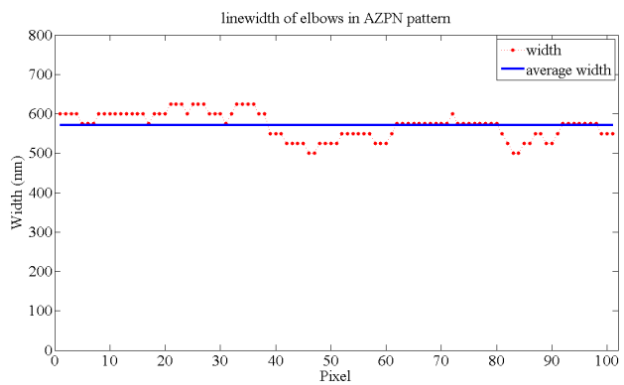


Fig. 4.5 a): Linewidth of elbows pattern in AZPN

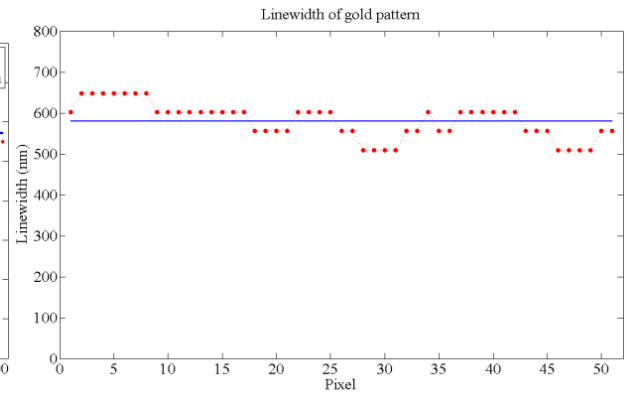


Fig. 4.5 b): Linewidth of Elbows pattern in Gold

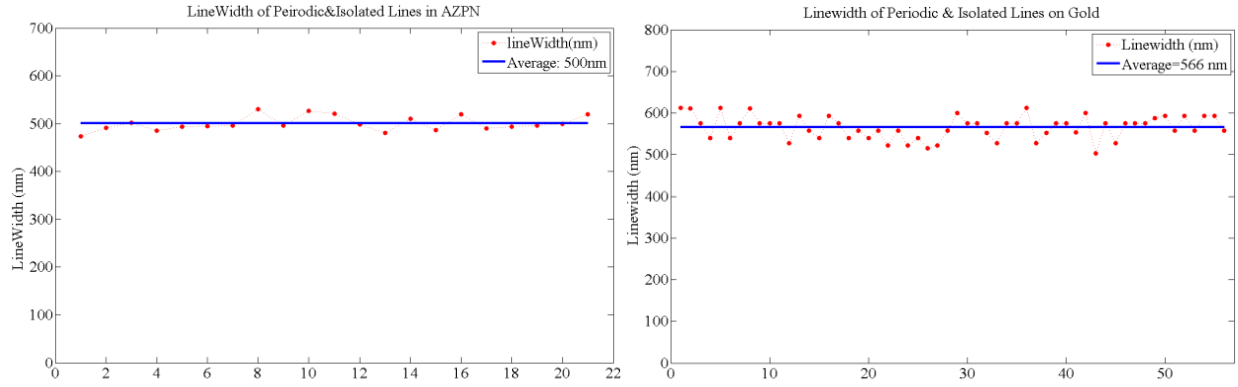


Fig. 4.6 a) (left): Linewidth of periodic & isolated lines in AZPN(AFM Cross Section)

Fig. 4.6 b) (right): Linewidth of periodic & isolated lines in gold measured by ImageJ (SEM)

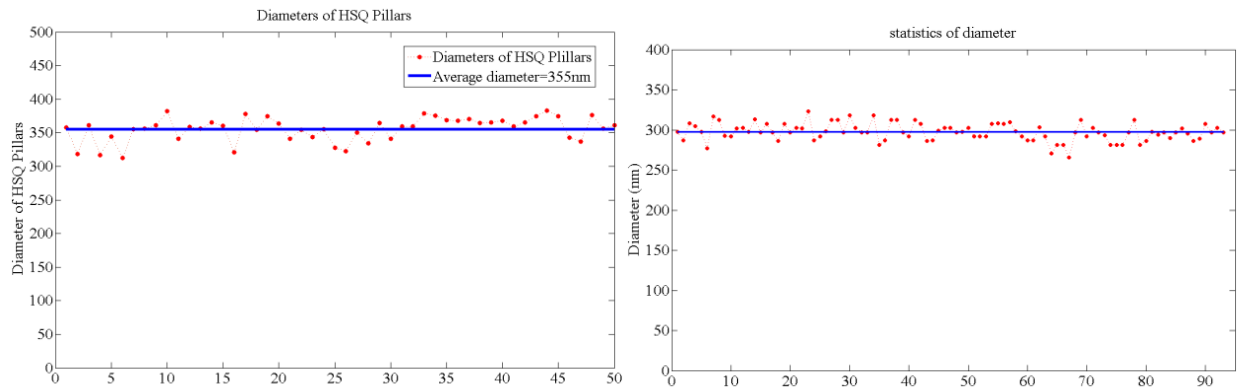


Fig. 4.7 a): Diameters of HSQ pillars with average 355 nm (measured by ImageJ)

Fig. 4.7 b): Diameters of gold pillars with average 297 nm (Measured by ImageJ)

From the results shown in section 4.3 and the analysis in section 4.4, it can be concluded that, EUV Talbot lithography using table top 46.9 nm laser is capable to print periodic structures in metal substrate over large area accurately. The defect free characteristic of the Talbot lithography was also demonstrated, producing defect free functionalized surfaces from heavily damaged masks.

#### 4.5 FUTURE WORK

The future work for this lithography technology has two objectives. One is to create smaller CD and the other is to enhance the aspect ratio.

#### 4.5.1 Double exposure to decrease CD

A concept of ‘double exposure’ is able to be used in this non-contact lithography to print smaller CD than the features on the mask. The schematic for this concept is shown in figure 4.8. By playing with the light intensity distribution together with the response curve of photoresist, a smaller CD than the one on the mask feature can be printed theoretically. Lines with 3 pixels wide are first printed by Talbot imaging followed by moving 1 pixel transversely and printing again with the same parameters. The dose of both exposures is half of the calibrated dose. The ultimate final intensity distribution from this double exposed Talbot imaging (shown in the blue line in figure 4.8), has therefore a smaller linewidth than the original.

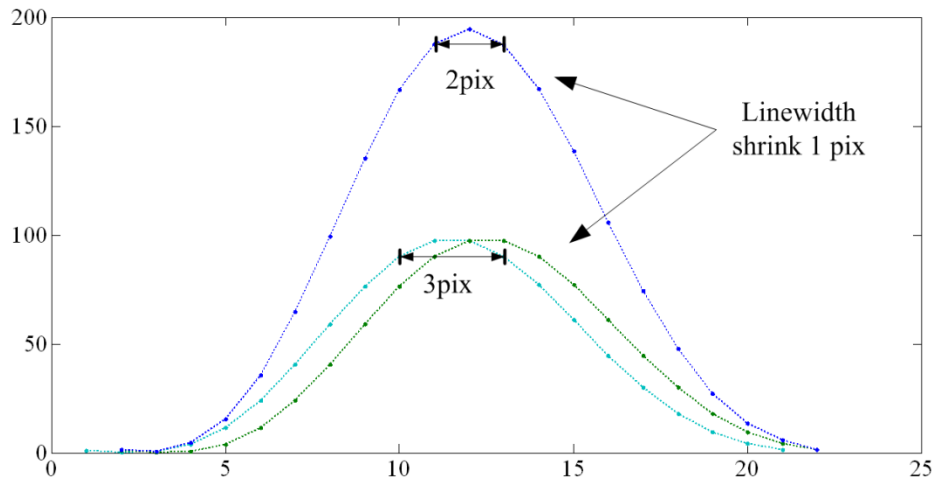


Fig. 4.8 Concept of double exposure

In fact, this concept is derived from edge definition <sup>[3,4]</sup>, in which the printable CD depends on the sharpness of the edges. For double exposure, the smallest printable CD depends on the resolution of the optical system and the response curve of photoresist. It can print smaller features from a mask with larger feature. Simulations of light intensity distribution of this concept are carried out and summarized in figure 4.9. The mask patterns (shown in figure 4.9 a)

used in the simulation are 100nm gratings separated by 400 nm space. Each cell is composed of 3 lines and the cell period is 2  $\mu\text{m}$ . Light intensity distribution for single exposure is shown in figure 4.9 b. After moving 40 nm (shown in figure 4.9 c) or 20 nm (shown in figure 4.9 d), the contrast of light intensity is change in a way that a smaller CD is achieved. For 40/20 nm movement, 40/20 nm linewidth can be printed if the threshold of photoresist response curve is sharp enough.

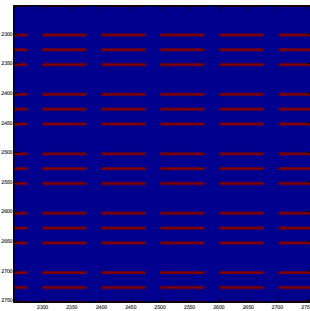


Fig. 4.9 a: mask pattern

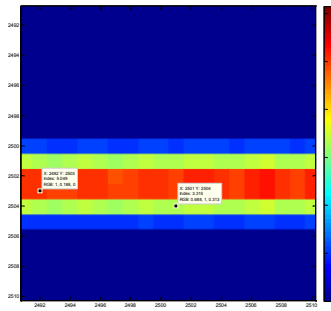


Fig. 4.9 b: single exposure

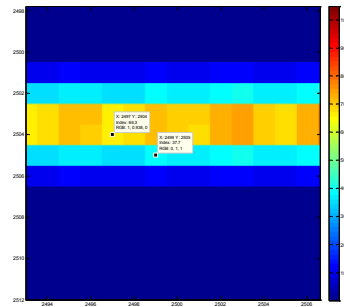


Fig. 4.9 c: 40 nm movement

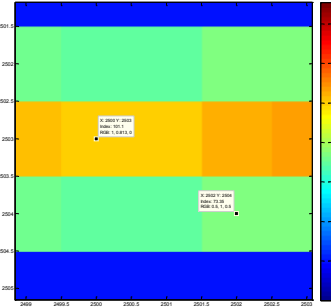


Fig. 4.9 d: 20 nm movement

A preliminary experiment was carried out to prove this theory using the mask shown in figure 4.10 a. The mask consists of gratings with 500 nm linewidth and separated by 700 nm. Photoresist PMMA was used in this experiment. The reconstruction without movement is shown in figure 4.10 b. The exposure dose for figure 4.10 b is 50 shots. In figure 4.10 c, the exposure dose is divided into 25+25 shots with a 200nm movement. The linewidth shrank to 320 nm.

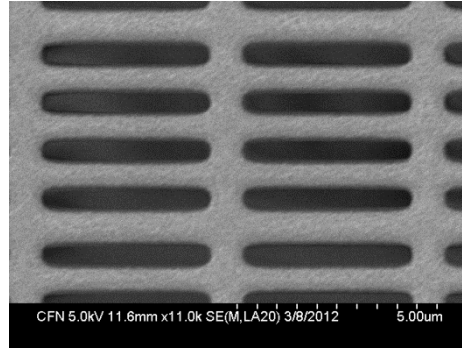


Fig. 4.10 a: Mask;

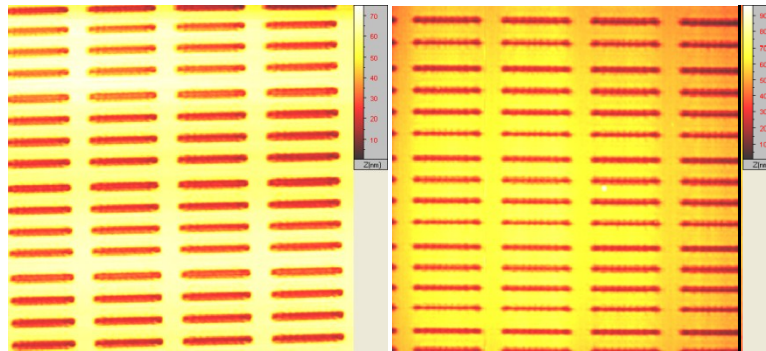


Fig. 4.10 b: original reconstruction with 50 shots; Fig. 4.10 c: Double exposure with 25+25 shots

#### 4.5.2 Sacrificial mask

To make a higher aspect-ratio feature, a Chromium sacrificial mask is needed. 20 nm Cr was evaporated on top of SiO<sub>2</sub> followed by spin-coating HMDS and 10 % AZPN. Masks shown in figure 4.10 a) were used in the set-up for Talbot imaging. After the AZPN gratings were fabricated, they were etched in the CAIBE to clean the residue of development. The purpose is to make sure that the Cr film is exposed to the following wet-etch process, in which, the patterns are transferred to Cr by Chromium etchant (Nitric acid HNO<sub>3</sub>). With Cr as sacrificial mask, a RIE (CF<sub>4</sub>) process was applied to etch the SiO<sub>2</sub> down. The process flow is shown in figure 4.11. The fabricated gratings are shown in figure 4.12. The height of the gratings is more than 1 μm.

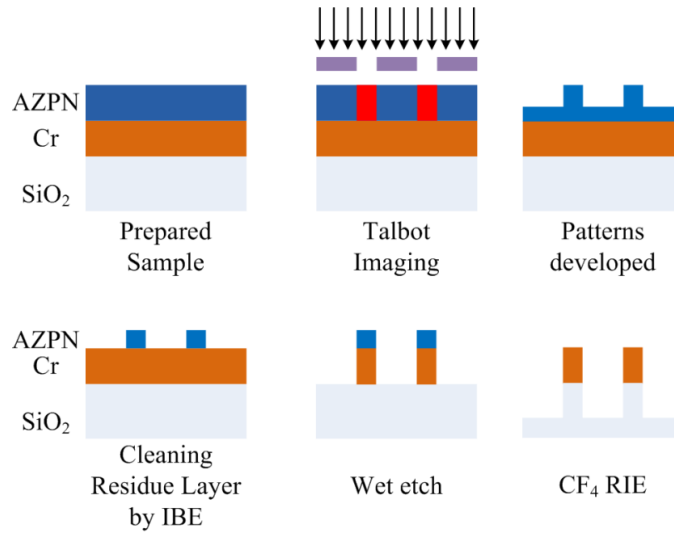


Fig. 4.11 Process flow for High aspect-ratio features

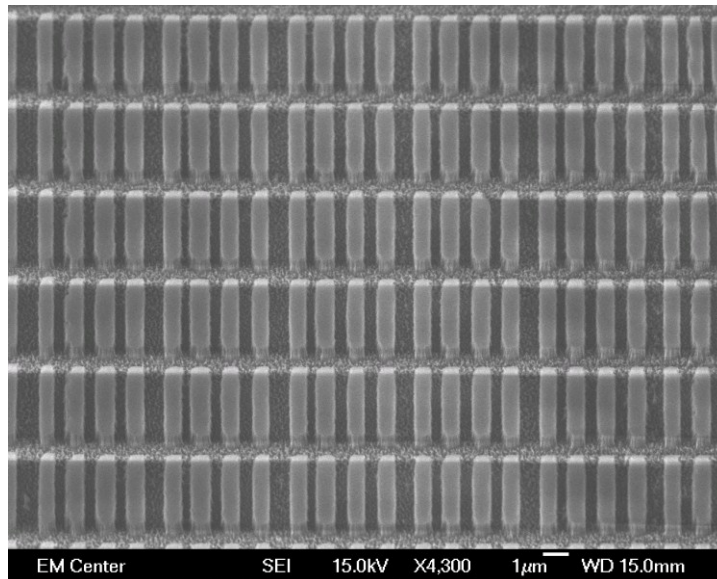


Fig. 4.12 Fabricated SiO<sub>2</sub> gratings

In future work, a mask with smaller cell periodicity will be fabricated to give a higher resolution and sharper edge. Sub 100 nm features with high aspect ratio will be reconstructed with this concept.

## 4.6 CONCLUSION

A promising nanofabrication method, which is capable of fabricating arbitrary periodic metal nanostructures in large area without defects, was proposed and experimentally proved. The fabrication of free-standing mask, experimental set-up for Talbot imaging and IBE process, preparation of the sample for EUVL and nanopatterns in photoresist & metal were shown in this work. Future plans to make nano-patterns with smaller features and higher aspect ratio were also demonstrated.

One unique characteristic of the approach is that it is capable to reconstruct defect-free patterns out of a heavily damaged mask. This non-contact EUV lithography can also utilize the concept of double-exposure to reduce the size of the printed feature by 50% on photoresist. The process with Cr sacrificial mask increased the height of SiO<sub>2</sub> features transferred from photoresist. Overall, nano-features with higher aspect ratio will be fabricated together with EUV Talbot lithography, double-exposure and sacrificial mask.

The combination of a compact EUV laser source with a classical optical effect enables the realization of a nano-patterning technique which is compact, efficient, cost-effective and defect tolerant. This thesis shows that Talbot lithography technique can be extended to shorter wavelengths and the pattern reconstructed to the photoresist is able to be transferred to metal substrate. It opens the possibility to further reduce the resolution of EUV Talbot lithography.

#### 4.7 REFERENCES

- [1] Weilun Chao, Jihoon Kim, Senajith Rekawa, Peter Fischer and Erik Anderson, 'Hydrogen silsesquioxane double patterning process for 12 nm resolution x-ray zone plates', *JVSTB* Issue 27 (2606), 2009.
- [2] Yanfei Shen, 'Comparison of two-typed (3-mercaptopropyl)trimethoxysilane-based networks on Au substrates', *Talanta*, Issue 65, 2005.
- [3] FLANDERS, DC, EFREMOW, NN, 'GENERATION OF LESS-THAN-50 NM PERIOD GRATINGS USING EDGE DEFINED TECHNIQUES', *J.V.S.T.B.* Volume 1, Issue 4, 1983.
- [4] S. Babin, and G. Glushenko, etc, 'Application of double patterning technology to fabricate optical elements: Process simulation, fabrication, and measurement', *J.V.S.T.B.*, 30(3), 2012.

## APPENDIX 1: MATLAB CODE FOR FRESNEL DIFFRACTION

### Basic Fresnel Propagator:

```

function talbot_75nmLine

tic

Ai=zeros(21000,21000);
Line=ones(75,21000);           %%%% 50nm line
Space=zeros(75,21000);        %%%% line:space=1:1
FirstPeriod=[Line;Space];     %%%% 50/50nm lines/spaces
period=100nm
Ai= repmat(FirstPeriod,21000/150,1);
figure(1)
imagesc(abs(Ai(12000:17001,12000:17001)));    %% sample the image
(5000*5000)
axis square
%%%%%%%%%%%%%%%%%%%%%%%%%%%%%%%%%%%%%%%%%%%%%%%%%%%%%%%%%%%%%%%%%%%%%%%%%%
%%%%%%%%%%%%%%%%%%%%%%%%%%%%%%%%%%%%%%%%%%%%%%%%%%%%%%%%%%%%%%%%%%%%%%%%%%

[Nx,Ny]=size(Ai);
dx=1e-9;%pixel size

dy=1e-9;%pixel size
lambda=46.9e-9;           %%%% wavelength of the propagator

Field=Nx*dx;
pp=150;                   %%%% cell size
%period=pp*dx=150nm
z_t=2*(dx*pp)^2/lambda;   %%%%%%%%%%% dx*150is
%the period and z=zT
%%%%%%%%%%%%%%%%%%%%%%%%%%%%%%%%%%%%%%%%%%%%%%%%%%%%%%%%%%%%%%%%%%%%%%%%%% try different z_t

NA=atan(Field/(2*(z_random)));
res=0.61*lambda/NA       %resolution
DOF=2*lambda/(NA^2)      %%% depth of focus

norm=1/sqrt(Nx*Ny);
[k,l] = meshgrid(-(Nx-1)/2:1:(Nx-1)/2, -(Ny-1)/2:1:(Ny-1)/2);

%%%%%%%%%%%%%%%%%%%%%%%%%%%%%%%%%%%%%%%%%%%%%%%%%%%%%%%%%%%%%%%%%%%%%%%%%%
%%%%%%%%%%%%%%%%%%%%%%%%%%%%%%%%%%%%%%%%%%%%%%%%%%%%%%%%%%%%%%%%%%%%%%%%%%

d= z_t;

kernel=exp(-1i*pi*(k.^2*dx^2+l.^2*dy^2)./(lambda*d));
%%%%%%%%%%%%%%%%%%%%%%%%%%%%%%%%%%%%%%%%%%%%%%%%%%%%%%%%%%%%%%%%%%%%%%%%%% Propagator

```

```

    %kernelR=exp(1i*pi*(k.^2*dx^2+l.^2*dy^2)./(lambda*d));
    %%%%%%%%% reverse propagator
    OUTi=norm*fftshift(iff2(fft2(Ai).*fft2(kernel)));
    %%%%%%%%% convolution of Ai and propagator is the Fresnel diffraction

    clear kernel;

figure(2);
imagesc(abs(OUTi(12000:17001,12000:17001).^2));
axis square
%%%%%%%%%%%%%%
%

% demonstration of double exposure in figure 3----- 1 dimensionally
%
% figure(3)
% plot(Temp(2495:2515,2308))
% hold on
% %
% Temp1=Temp(2495:2515,2308);
% plot(2:1+length(Temp1),Temp1)
% for i=1:length(Temp1)-1
%     Temp1(i)=Temp1(i)+Temp1(i+1);
% end
% plot(2:1+length(Temp1),Temp1)
% plot(0.95.*194.*ones(1,length(Temp1)))
% plot(0.9.*97.*ones(1,length(Temp1)))
% %
% hold off

toc

```